Hybridization and Covalency in the Group 2 and Group 12 Metal Cation/Rare Gas Complexes

William D. Tuttle,[a] Joe P. Harris,[a,b] Yu Zheng,[a] W. H. Breckenridge[c] and Timothy G. Wright*[a]

[a]School of Chemistry, University of Nottingham, University Park, Nottingham, NG7 2RD. UK

[b] Present address: Département de Chemie, Université de Montréal, Montréal QC H3C 3J7, Canada

[c] Department of Chemistry, University of Utah, 315 S. 1400 East Rm. 2020, Salt Lake City, UT 84112, USA

* Tim.Wright@nottingham.ac.uk; +44 (0)115 8467076

ABSTRACT

We provide a consistent set of interaction energy curves for the Group 2 (IIA) and Group 12 (IIB) metal cation/rare gas complexes, M^+-RG, where $M^+ = Be^+–Ra^+$ and $Zn^+–Hg^+$; and RG = He–Rn. We report spectroscopic constants derived from these, compare them with available data, and discuss trends in the values. We gain insight into the interactions that occur using a range of approaches: reduced potential energy curves; charge and population analyses; molecular orbital diagrams and contour plots; and Birge-Sponer plots. Although sp hybridization occurs in the Be^+-RG, Mg^+-Rg and Group 12 M^+-RG complexes, this appears to be minimal and covalency is the main aspect of the interaction. However, major sd hybridization occurs in the heavier Group 2 M^+-RG systems, which increases their interaction energies but there is minimal covalency. Examination of Birge-Sponer plots reveals significant curvature in many cases, which we ascribe to the changing amounts of hybridization or covalency as a function of internuclear separation. This suggests why the use of a simple electrostatics-based model potential to describe the interactions is inadequate.

1. INTRODUCTION

Interactions between metal cations and rare gas atoms are the simplest systems with which to investigate molecular interactions that can be viewed as underpinning catalysis as well as many bioinorganic processes. Studies of such systems allow detailed insight into the very weakest of interactions with the He atom, through to incipient chemical bonding with Xe and Rn. As the interactions become stronger, we expect initial distortion of the electronic clouds (physical interactions), through to hybridization and eventually full covalent bonding. Being able to study families of systems where these regimes are traversed is expected to increase our understanding of chemical bond formation. As such, many theoretical studies have been undertaken previously by our group on M^+-RG systems (RG = He–Rn), with the metals coming from Group 1,[1,2,3,4,5,6] Group 2,[7,8,9] Group 11,[10,11] Group 12,[12,13] and Group 13.[14,15,16,17] These studies have used CCSD(T) or RCCSD(T) theory with large basis sets to calculate interaction energy, E_{int}, curves (IECs), often extrapolated to the basis set limit. These IECs have been employed to obtain spectroscopic constants and to calculate transport coefficients for the metal cations moving in inert gases. At the commencement of the studies, the emphasis was on obtaining reliable IECs with a view to generating transport coefficients to compare to experiment, and to the limited spectroscopic data available. However, in a number of cases it was evident that the systems were showing behaviour that was reminiscent of incipient chemical bonding, and so various methods were employed to establish the extent to which "chemistry" was present in the interactions, as opposed to just "physics". (Here, the use of the term "chemistry" includes covalency and also hybridization that occurs as a result of the interaction.) Initially, this was undertaken using a physical "model potential" [18] also including damping,[1,6] but we have since employed various population analyses, as well as molecular orbital diagrams including contour plots. Also, it has recently proven insightful to look at Birge-Sponer plots of the whole set of calculated bound vibrational levels,[15] as this seems to show subtleties in the change in shape of a IEC that are otherwise difficult to see, even using such approaches as reduced potentials.[9,15] Finally, contour plots and molecular orbital diagrams allow the visualization of the interactions between the atomic orbitals.[9,15] In the present work, we apply the most insightful of the above methods in an examination of the interactions of the Group 2 (Be^+–Ra^+) and Group 12 (Zn^+–Hg^+) metal cations with each of the rare gases (He–Rn).

Of the systems previously studied, the metal cations belonging to groups 1, 11, and 13 all possess $^1\Sigma^+$ electronic ground states, and as such it might have been anticipated that the interactions within those M^+–RG complexes would be of essentially the same character. However, as previous investigations have highlighted, interactions in the Group 11 M^+-RG complexes exhibit rather strong binding energies,[10] with Au^+-Xe in particular being very strongly bound and proposed as exhibiting a degree of covalency.[11,19] Conversely, the Group 1 complexes are comparatively weakly bound and were found to be described well by a 'physical' model potential that included the main induction and dispersion terms together with a simple repulsion potential.[1,6] Group 13 is a different case again, with the heavier

members of the M^+-RG group showing similar behaviour to the Group 1 complexes,[16] and the lightest members, involving B^+,[17] showing strong binding energies with some incipient covalency.

Another logical comparison presents itself in the case of the Group 2 and Group 12 M^+–RG complexes. For these complexes, a single unpaired electron is present in the outermost valence *n*s orbital, and as such these all possess common $^2\Sigma^+$ electronic ground states. Consequently, on the basis of valence isoelectronic arguments, the complexes from both of these groups might be expected to exhibit close similarities in their interactions. In previous work we have examined the Group 2 complexes in detail[7,8,9] but not consistently with all of the above-described methods. Unfortunately, at that time, consistent basis sets were not available for the whole set of Group 2 metals and so custom-designed ones were employed in some cases, albeit to match the quality of standard Dunning-style aug-cc-pV5Z basis sets combined with an effective core potential for the heavier species. A similar situation occurred with the Group 12 species,[12,13] but also at that time a detailed analysis of the interactions was not undertaken.

In the present work, we firstly report high-quality IECs, employing consistent basis sets across the whole set of complexes and extrapolating to the basis set limit. Furthermore, we undertake analyses of the interactions across the series using various approaches, which allow us to compare and contrast the interactions in these valence isoelectronic species.

2. COMPUTATIONAL DETAILS

As noted above, some of our previous studies on the Group 2 and Group 12 M^+-RG complexes employed custom-designed basis sets of the same overall construction as the Dunning-style quintuple-ζ quality basis sets. Since then, appropriate basis sets have subsequently been published for all relevant metals[20,21,22] and we have now undertaken RCCSD(T) calculations with these to obtain consistent IECs for all of the complexes; further, since both quadruple-ζ and quintuple-ζ quality basis sets became available, we could also extrapolate the interaction potentials pointwise to the complete basis set limit using the X^{-3} method of Halkier et al.[23] In our earlier work on Be^+-RG and Mg^+-RG,[9] the basis sets employed were pre-publication versions, and these were slightly modified in their published form, and so those calculations were repeated using the published basis sets, for consistency.

RCCSD(T) IECs for each of the 54 complexes have been calculated using MOLPRO,[24] covering a range of internuclear separations that covered the long- and short-range as well as equilibrium separation regions. The final extrapolated curves may be represented as RCCSD(T)/apCV∞Z or RCCSD(T)/apwCV∞Z quality. LeRoy's LEVEL 8.0 code[25] was then employed to obtain rovibrational energy levels from each of these curves. A number of spectroscopic constants were then obtained from standard Morse expressions, as discussed below. Birge-Sponer-like (BS) plots were created using the calculated separations between the vibrational levels.

The details of the basis sets employed for the metals are as follows (with X = Q, 5): for beryllium and magnesium, all-electron aug-cc-pwCVXZ (weighted-core); for Ca, Sr and Ba aug-cc-pCVXZ-PP (non-weighted-core) valence basis sets along with relativistic, small-core effective core potentials ECP10MDF, ECP28MDF and ECP46MDF, respectively; and for Zn, Cd, Hg and Ra aug-cc-pwCVXZ-PP valence basis sets with relativistic, small-core effective core potentials ECP10MDF, ECP28MDF, ECP60MDF and ECP78MDF, respectively. For the rare gases, aug-cc-pVXZ basis sets were used for He, and for Kr–Rn aug-cc-pwCVXZ-PP valence basis sets were employed with small-core effective core potentials ECP10MDF, ECP28MDF, and ECP60MDF, respectively. For Ne and Ar, either aug-cc-pCVXZ or aug-cc-pwCVXZ basis sets were used to match whether a core-weighted basis set was used for the metal cation or not. The use of either core-valence or weighted-core-valence basis sets is not expected to impact the results significantly, with any effect having even less impact on interaction energies. In our previous work on the Be^+-RG and Mg^+-RG complexes, we employed doubly-augmented basis sets, thus giving a better description of the diffuse regions of electron density. Although we mostly employ singly-augmented basis sets here, we found that in several cases there was a requirement for the second set of diffuse functions; hence, as will be discussed below, in those cases we present RCCSD(T)/d-aCV∞Z results.

For Be^+ all electrons were correlated, while for Mg^+ all but the 1s electron were correlated; for the heavier Group 2 metals, all electrons on the metal not described by the ECPs were correlated. In the cases of the rare gas atoms, the Ne 1s orbitals and Ar 1s, 2s, and 2p orbitals were frozen. Each of the heavier rare gases RG = Kr–Rn had the inner-valence (*n*-1)s and (*n*-1)p orbitals frozen. As regards Group 12, each of the metals Zn–Hg had only their inner-valence (*n*-1)s orbitals frozen, since the (*n*-1)p orbitals for these cations are higher in energy than the analogous Group 2 cation orbitals, and all other electrons (save for those described by the ECP) were correlated. The same correlation scheme that was used for the rare gas atoms in the Group 2 complexes was also used for Zn^+-RG and Cd^+-RG, and also for the Hg^+-He, Hg^+-Ne, and Hg^+-Ar complexes, but the 5p orbitals on the mercury cation are energetically closer to the inner-valence orbitals for RG = Kr–Rn. As such, for those three complexes the inner-valence Hg^+ 5s orbital was frozen, and all others outside of the ECPs (including those on the rare gas) were correlated.

Orbital contour plots were also produced for these complexes: the orbital energies were taken from Hartree-Fock calculations performed using triple-ζ basis sets of the same designation as those used for the IEC calculations; the equilibrium separation employed was that obtained using the CCSD(T)-extrapolated basis set results. Calculated contours were visualized using MOLDEN.[26]

Partial atomic charges were obtained using Mulliken populations,[27] natural population analysis (NPA),[28] and the atoms-in-molecules (AIM)[29] theories. For the NPA and AIM analyses, we analyzed the density from QCISD calculations performed with Gaussian 09[30] using the same triple-ζ basis sets

as just noted. The NPA analysis used the NBO6 software,[31] whilst the AIM analysis used AIMAll.[32]

3. RESULTS AND DISCUSSION

A. IECs and Spectroscopic Constants

The IECs are plotted in Figure 1 for the Group 2 M^+-RG complexes, and in Figure 2 for the Group 12 M^+-RG complexes. Full interaction energy curves are provided as Supplementary Material for all species. A summary of the derived spectroscopic constants obtained from the IECs are provided in Table 1 for the Group 2 complexes, and Table 2 for the Group 12 complexes. The key experimental data[33,34,35,36,37,38,39,40,41,42,43,44,45,46,47,48,49,50,51,52] are displayed in Tables 1 and 2, as well as comparisons between the present and our previous work. Since these complexes have been previously studied using subsets of the approaches taken here, and in those studies generally very good agreement between previous theoretical and experimental work was seen,[6,7,8,9,12,13] a full survey of previous experimental and theoretical studies is not repeated herein. In most cases, those experimental results are spectroscopic studies and it was possible to compare to the calculated spectroscopic constants. The previous IECs from our group for the titular species were also used to calculate ion transport coefficients and this provided another avenue of comparison by which to evaluate the quality of the calculated potentials via ion transport studies of metal cations moving through a bath of rare gas.[7,8,9,12,13] Some comment will, however, be made on several studies that have been published since that earlier work.

For the Be^+-RG and Mg^+-RG complexes, the new IECs are almost identical to those published previously[9] (since there were only minimal changes to the basis sets between the two studies). We noted in that work that for Be^+-Ar and Be^+-Kr particularly, but also for Be^+-Xe, high-quality spectroscopic information is available from Coxon et al.[33,34,35] In Ref. 9, we compared to the experimental rotational and vibrational constants and obtained excellent agreement. There, we used the v = 0, 1 and 2 energies to derive the standard Morse (ω_e and $\omega_e x_e$) constants; and B_0 and B_1 values to obtain the B_e and α parameters – this method mimics that used in a spectroscopic experiment. In the present work, we note that R_e and D_e can be obtained from the interpolated IEC from the LEVEL program. The R_e value allows the calculation of B_e and together with B_0, we can obtain α ; similarly, with D_e and the v = 0 and 1 energies, the Morse vibrational constants can be obtained. The latter approach should be more representative of the lowest regions of an IEC and so more representative of the curvature there – we report the results from this approach in Tables 1 and 2. As an example, for Be^+-He, we obtain B_e = 0.7189 cm^{-1} and α = 0.1175 cm^{-1} from the latter approach, but the corresponding values are 0.7242 cm^{-1} and 0.1420 cm^{-1} using the former. The differences between the two approaches become less marked as the well depth increases, as expected. Even though these two slightly different methods have been used to obtain the spectroscopic constants, the agreement of the present results with our previous calculated values, and the limited available experimental spectroscopic ones, is excellent (see Table 1).

In Ref. 9 we ran calculations with doubly-augmented basis sets. Here, for Be^+-Ne, we ran sets of calculations with singly-, doubly-, and triply-augmented basis sets, with the latter obtained in an even-tempered way from the former. We found that the double-augmentation gave results that were significantly different from the singly-augmented ones, while the triple augmentation essentially gave no further improvement. Thus, for Be^+-Ne we conclude that doubly-augmented basis sets are required to give converged results and these are the ones presented in Table 1. With this in mind, we also performed the same set of calculations for Be^+-Ar, and obtained no further improvement over the singly-augmented basis set, and so use the latter results in further analyses. In fact, double augmentation of the basis set was only important for the Be^+-Ne and Mg^+-Ne species.

Table 1 shows selected available experimental results for M^+ = Mg^+, Ca^+, Sr^+ and Ba^+; there are no experimental data for M^+ = Ra^+. Generally the close agreement between the previous and present spectroscopic parameters means that the previous comments[7,8] apply. We are aware of only a few studies published on the Group 2 M^+-RG complexes subsequent to our previous work.[9] Three of these are focused on a single Group 2 M^+-RG complex, Be^+-Ar[53], Be^+-Kr[54] and Ba^+-Xe[55]; while a more recent study tackled the Ba^+-RG series, for RG = He–Xe.[56]

The very recent study on Be^+-Ar by Niu et al.[53] used CASSCF/icMRCI+Q calculations in conjunction with both triple- and quadruple-ζ quality Dunning-style basis sets, allowing extrapolation to the basis set limit. Several electronic states were calculated and spectroscopic constants derived for each state. For the ground state, D_e was reported as ∼4030 cm^{-1}, which is significantly lower than the values obtained in the present and our previous work;[9] the agreement for R_e is fairly good, albeit with a shorter value of 2.065 Å compared to that reported here, with our value being in excellent agreement with that of the previous spectroscopic study[33] of 2.086 Å. We note that the given units (cm^{-1}) for the D_e value in Ref. 53 are incorrect, and should be eV; converting the given value to cm^{-1} then yields a value of 4380 cm^{-1}, which is in fairly good agreement with the present value, albeit lower. Other given spectroscopic constants are also in fairly good agreement, but our values are in excellent agreement with experiment throughout. On the other hand, for Be^+-Kr, the D_e value in ref. 54 of 6180 cm^{-1} is slightly larger than the value obtained here, while the R_e value of 2.232 Å is slightly longer than the present value and the spectroscopic value[34] – see Table 1. With regard to the other constants, ω_e and B_e agree well, but $\omega_e x_e$ and α are in somewhat poorer agreement with our previous and spectroscopic values. We conclude that the MRCI calculations of Ref. 54 are somewhat compromised in their description of the $X^2\Sigma^+$ ground state, owing to their state-averaged nature; additionally, the basis sets used in the present work are larger, making the extrapolation to the basis set limit more reliable.

The study on Ba^+-Xe by Abdessalem et al.[55] used a pseudopotential plus core-polarization function for the Ba^{2+}-Xe 'core'. In that work only the lone 6s electron was active in the configuration interaction treatment, which was used to calculate several electronic states of Ba^+-Xe (and Ba-Xe). For the ground

state of Ba^+-Xe, the reported equilibrium separation showed poor agreement with our value, with theirs being 3.77 Å compared to the present CCSD(T) result of 3.581 Å. Similarly poor agreement is seen in the values for D_e, as the value reported by Abdessalem is 1971 cm^{-1}, significantly higher than the present result of 1731 cm^{-1}.

Very recently, Buchachenko and Viehland[56] studied the Ba^+-RG series as part of a wider study of the interactions of the rare gases with neutral, singly- and doubly-charged barium atoms. A range of different basis sets were employed, with the calculations being carried out at the RCCSD(T) level. Various sizes of Dunning-type basis sets were employed, with and without bond functions; additionally, for the cases where an ECP was employed, small-core versions were also tried. These calculations are very similar to those employed here: we also employ the RCCSD(T) method, and employ the corresponding Dunning-type basis sets, and small-core ECPS. Extrapolation to the basis set limit was performed in Ref. 56, with and without bond functions, but not with the small-core ECPs. In addition, the radon-containing complexes were not considered. When we compare the results in Table 1 to those in Ref. 56, we find excellent agreement for both R_e and D_e for each of Ba^+-He and Ba^+-Ne, with the extrapolated results that employed the non-bond function basis sets, while for RG = Ar–Xe, our R_e values are slightly shorter and the D_e values slightly larger. The decreasing trend of R_e and the increasing trend of D_e with improvements in the basis set in Ref. 56, suggests that the present results are likely the more reliable. There are experimental spectroscopic and transport data available for Ba^+-Ar (see Table 1). The agreement for R_e from Ref. 56 is slightly closer to the experimental value, but the values of the dissociation energy from Ref. 56 and the present value suggest the spectroscopic estimate[51] is a little low, and that the transport value[52] is more in line with the calculated values. With regard to the vibrational parameters, the ω_e value from Ref. 56 is in slightly better agreement with experiment, while the present $\omega_e x_e$ is better. Overall, the results from the present study and those of Ref. 56 may be regarded as being of a similar reliability.

Note that the present $\omega_e x_e$ value for Ba^+-Xe is significantly smaller than that from our previous work[7] and also that from Ref. 56. We checked this, and we find that values from the two unextrapolated potentials are in good agreement with the previous values, but the extrapolated IEC leads to this smaller value; since there are no experimental data for this complex, further evaluation cannot be made.

No studies subsequent to our previous work[12,13] seem to have been published for $M^+ = Zn^+$–Hg^+.

B. Reduced Potentials

It may be seen from Figures 1 and 2 that it is difficult to compare the bonding directly from the IECs, since the binding energies are very different and changes to the shapes of the curves are not apparent. In Figures 3 and 4 we show reduced potential plots,[57,58,59,60] where the interaction energies are normalized to D_e and the internuclear separations to R_e, making any difference in the shapes of the IECs

more evident. Such plots are expected to be close to each other for a family of species, if the interactions are similar; any differences can be attributed to differences in the interactions, and so have implications for whether a universal diatomic potential function exists.[61,62] As may be seen for the Group 2 M^+-RG complexes, the M^+-Ne curves are markedly different from the others, being significantly flatter. We examined such plots for Be^+-RG and Mg^+-RG in Ref. 9. There it was noted that Be^+-Ne was unusual; however, it is clear from Figure 3 that the M^+-Ne species are somewhat out of line for all of the Group 2 complexes. In contrast, the reduced potentials for the Group 12 M^+-RG species in Figure 4 are all somewhat similar. The implication from the reduced potential plots is that the repulsive region of the Group 2 M^+-Ne complexes is comparatively more important at R_e than for the other species, and particularly so for Be^+-Ne – we shall come back to this point later.

Another way of examining the interactions is via the κ parameter[58] (which is essentially the Sutherland parameter put forward in 1938),[63] which has been termed the "reduced curvature of the potential at R_e",[58] and may be expressed as:

$$\kappa = \omega_e^2/2B_eD_e \qquad (1)$$

The κ values for the Group 2 and Group 12 M^+-RG complexes are given in Table 3 and plotted in Figure 5. It may be seen that the Group 2 M^+-Ne complexes have κ values that are significantly different to the other species, in line with their different reduced potentials. In contrast, for the Group 12 M^+-RG complexes, the κ values fall in a narrower range, although the values for Hg^+-RG are somewhat more erratic. Winn[58] has noted that κ values in the range 0–20 are indicative of strong chemical bonding, which would seem to include Be^+-Ne, with the heavier Be^+-RG complexes having values close to this range. This does not fit with the relatively weak binding in these complexes and indicates that κ values should only be used in a comparative way within groups of similar species, rather than as a global indicator. For the Group 2 complexes, there is an overall increase and plateauing of the κ values as the atomic number of M^+ increases, with the Ba^+-containing complexes being unusual. With regard to the atomic number of RG, there is a fall from He to Ne for all complexes. There is then a gradual rise and plateauing for the other RG atoms when $M^+ = Mg^+$–Sr^+ and Ra^+, while the Be^+-RG and Ba^+-RG complexes have the opposite trend for RG = Ar–Rn.

For the Group 12 species, there is a rise of κ with the atomic number of M^+. Additionally, there is an overall fall in κ with the atomic number of RG, although the trend is somewhat erratic. It is interesting to note that for RG = Ar–Rn, the Be^+-RG and Ba^+-RG trends are similar to those of the corresponding Group 12 species.

Overall, we feel that the κ parameter has limited use, and the reduced potential plots themselves seem

more transparent in highlighting differences in the interactions. We make a further comment on the κ parameter at the end of the following subsection.

C. Trends in the Spectroscopic Constants of the Group 2 M^+-RG Series

Equilibrium Internuclear Separations

In Figure 6 we plot the R_e values for the Group 2 and 12 M^+-RG to allow an examination of trends in the values. First, it is clear (see also Tables 1 and 2) that the Group 12 species generally have shorter bond lengths than their corresponding Group 2 counterparts along the same row of the Periodic Table. Next, we note that for the same RG atom, the R_e values generally show an overall increase with increasing atomic number of the metal cation for the Group 2 M^+-RG complexes. This increase is mostly monotonic with the increasing atomic number of the metal, but for RG = Ar–Rn, a small dip is seen at Ba^+

Examining now the trends throughout each M^+-RG series as the rare gas atom is changed, for the Group 2 species a uniform behaviour is seen for all series, marked by a decrease from RG = He through Ar, followed by an increase thereafter. We interpret this in terms of a subtle balance between the attractive and repulsive terms. From helium through argon, the rate at which the attractive terms increase with R evidently outpaces the increase in repulsive terms, leading to successively contracting bond lengths. From argon onwards, however, the repulsive terms are seen to be becoming relatively more important and so the equilibrium separations increase in response. It is clearly surprising that there is the fall from He to Ar, since the RG atom is becoming larger and this will be discussed later.

For the same RG atom, the M^+-RG complexes involving the Group 12 metals all show similar behaviour, in that the Cd^+-RG complexes show the longest bond lengths in each case and the Zn^+-RG complexes the shortest, with the Hg^+-RG bond lengths close to those of Zn^+-RG for the lighter RG atoms. A rationale for this arises through consideration of the ionic radii of the metal cations, for example using the Wright-Breckenridge radius, R_{WB},[64] whereby an estimate for the ionic radius of a cation is found by subtracting half the He_2 dimer equilibrium separation, (1.49 Å) from the value of M^+-He. For the Group 12 metal cations, this treatment leads to the ordering of the ionic radii being $Cd^+ > Hg^+ \gtrsim Zn^+$ – a result which is in line with the lanthanide and relativistic contraction experienced by mercury, and accounts for the observed trends.

Examining each Group 12 M^+-RG series for a fixed M^+, a rather different picture is seen, which is similar to the trends seen for the Group 2 complexes, albeit less pronounced. For all three series, there

is an initial decrease in bond length as the atomic number of the rare gas increases, followed by a rise for the heavier rare gases, with the turning point being at M^+-Ar for Zn^+-RG and Cd^+-RG, but at Kr for Hg^+-RG. The same explanation given above for the Group 2 species is applicable, in that there is a balance between the attractive and repulsive terms in each complex.

Dissociation Energies and k

In Figure 7 we plot the D_e values for the Groups 2 and 12 M^+-RG, and it may immediately be seen that the Group 12 (M^+=Zn^+–Hg^+) species have larger dissociation energies than their corresponding Group 2 (Ca^+–Ba^+) counterparts.

There is a general trend in the D_e values of decreasing dissociation energy with increasing atomic number and size of the metal cation, this is in line with the leading term, $-\alpha/2R^4$, of the ion/induced-dipole interaction. In the case of the lightest two rare gases, there are much sharper decreases in interaction energy seen for the lighter metal cations, which eventually give way to the more-slowly changing interaction energies for M^+ = Ca^+–Ra^+. Notably there is a very small increase in dissociation energy at Ba^+-RG.

For the heavier rare gases, the interaction energies are generally much higher than for the He and Ne analogues and the rise is particularly steep for Be^+-RG. The explanation of this is the small size of Be^+, which allows the close approach of RG and so a significant increase in the attractive electrostatic terms, in particular the leading charge/induced-dipole term, $-\alpha/2R^4$.

Trends for the harmonic vibrational frequencies, ω_e, are usually generally less clear since the harmonic vibrational frequencies are a consequence of two main effects: the electronic interaction and the reduced mass of each system. Hence, we focus on the trends in the force constant obtained from Hooke's law, k, and these are plotted in Figure 8 for both the Group 2 and Group 12 M^+-RG complexes. The trends in k are very similar to those in D_e, as might be expected.

Comment on κ

We noted above that the κ parameter was quantitatively not very indicative of the bonding in these species. We have noted in the above subsections that the variation in these parameters can be quite marked and is not always monotonic. It may be seen from its definition (Equation 1) that it depends on ω_e, R_e (via B_e) and D_e. As such, the κ parameter depends on different aspects of the interaction, both at R_e and at the dissociation asymptote; when we consider Birge-Sponer plots and discuss the contour plots of the molecular orbitals later on, it will become more obvious that linking κ to the strength of bonding is simplistic.

D. Molecular Orbital Diagrams and Contour Plots

In discussing the interactions in the M^+-RG complexes, it will be useful to refer to the energies of some of the lowest M^+ excited states, which are presented in Table 4 and are taken from Ref. 65.

Be^+-RG and Mg^+-RG

We present molecular orbital diagrams and associated contour plots in Figure 9 for Be^+-RG and Mg^+-RG (RG = He, Ar and Xe). For all RG, ϕ_1 corresponds largely to the outermost *n*s orbital on RG – it appears at a significantly lower energy in the complex than on the isolated RG atom, since in the cationic complex it experiences the coulombic field from M^+, which lowers its energy, but this is ameliorated by e^-–e^- repulsion. In the case of M^+-He, it can be seen that ϕ_2 is largely the outermost *n*s orbital on M^+ and is at almost the same energy in the complex and in the atomic cation. For RG = Ar and Xe the situation is a little more complicated as there are now four molecular orbitals made up from the interactions between the outermost *n*s orbital on M^+ and the outermost *n*p orbitals on RG. (We neglect the expected small contributions from the outermost *n*s orbital on RG.) Note that there will be a loss of degeneracy of the three MOs that largely correspond to the three RG *n*p orbitals (ϕ_2–ϕ_4) from the interaction with the positive charge on M^+. Further deviations may then occur as a result of covalency, which will be accompanied by a concomitant rise in the energy of ϕ_5 from the atomic energy of the outermost *n*s orbital on M^+, making this orbital antibonding in nature. The latter clearly destabilizes the overall interaction, but this is balanced by the other stabilizing interactions that occur. These deviations in the orbital energies are clearly significant. Although ϕ_5 is predominantly the outermost M^+ *n*s orbital, there is clearly an interaction with the outermost RG *n*p orbital; although less clear from the contours, there is also a small amount of M^+ outermost *n*s character in ϕ_2. Further, there are small contributions to ϕ_5 from the formally unoccupied M^+ (*n*+1)p orbitals, which arise from the sp hybridization of the metal centre; this will lead to ϕ_5 being stabilized, reducing its antibonding character. This effect is only slight since the excited M^+ p orbitals are relatively high in energy (Table 4). The effect of this small amount of sp hybridization is to facilitate the movement of electron density away from the internuclear region and so reduce the electron repulsion between the electron in the M^+ *n*s orbital and the incoming RG atom; this also allows RG to approach the M^+ core more closely, increasing the various attractive electrostatic terms, as well as allowing RG to see a higher effective nuclear charge. The sp hybridization effects can be discerned in minor perturbations to the contour plots of the M^+ electron density on the side opposite to the RG atom. The overall effect of the covalency and sp hybridization is a clear stabilization of the interaction. It is notable that the extent of these effects seem to be similar for the Ar and Xe complexes: increased degrees of interaction would seem to require a distortion of the inner regions of the singly-occupied *n*s orbital and the latter is clearly more strongly held by the nuclear charge and we conclude the energy cost of this is too high to be recouped from increased charge/induced-dipole terms arising from moving the RG atom closer. Similar comments

apply to the Mg^+-RG complexes, but to a much lesser extent; this can be attributed to the larger size of the Mg^+ ion, which means that the amount of energy gained from attractive interactions with the RG atoms is lower, because of the leading $-\alpha/2R^4$ ion/induced-dipole interaction.

Comparison of Interactions in Groups 2 and 12

In Figures 10–12 we show comparisons of the Group 2 M^+-RG complex with the Group 12 species located along the same period. We start by considering the MO diagram for Ca^+-He in Figure 10, where ϕ_1–ϕ_3 almost entirely correspond to the Ca^+ atomic 3p orbitals, ϕ_4 to the He 1s orbital (but lowered in energy owing to the coulombic field) and ϕ_5 to the Ca^+ 4s orbital. In the case of Zn^+-He, the same picture may be seen to apply, except the penultimate occupied orbitals on Zn^+ are the 3d orbitals, which are almost entirely degenerate. Note that ϕ_6 is coincidentally very close in energy to ϕ_1–ϕ_5, and arises from the coulombically-lowered He 1s orbital; however, the lowering in energy of ϕ_1 is minimal, suggesting this interaction is weak, even though the contours show mixed character. It may be seen that ϕ_7 is largely the unperturbed Zn^+ 4s orbital. Reference to the M^+-He diagrams helps us to orient ourselves when considering the M^+-Ar and M^+-Xe MO diagrams, with the observation that the coulombically-lowered RG *n*s orbital becomes ϕ_1 for Zn^+-Ar and Zn^+-Xe, and ϕ_2–ϕ_6 are the (*n*-1)d orbitals. First, we note that for Ca^+-Ar and Ca^+-Xe ϕ_1–ϕ_3 stay approximately degenerate, and this is also the case for ϕ_2–ϕ_6 for Zn^+-Ar and Zn^+-Xe; consequently, we can conclude that these orbitals remain atom-localized and are largely unaffected by the complexation. However, ϕ_5–ϕ_7 for Ca^+-Ar and Ca^+-Xe, and ϕ_7–ϕ_9 for Zn^+-Ar and Zn^+-Xe lose their degeneracy, and further, there is a rise in energy of ϕ_{10}, suggesting covalency. Moreover, ϕ_8 in both Ca^+-Ar and Ca^+-Xe shows off-axis 3d contributions, arising from sd hybridization.

In contrast, for the Zn^+-RG systems the main effect appears to be covalency, with interaction between the M^+ 4s and the RG outermost np_z orbitals, causing ϕ_7 to lower in energy; there is also a rise in energy of ϕ_{10}. In the cases of Zn^+-Ar and Zn^+-Xe there are small perturbations to the contour plots of ϕ_{10} on the side opposite to the incoming RG atom, arising as a result of very small amounts of sp hybridization; these are small, however, owing to the relatively high energy of the M^+ excited p orbitals (Table 4). Small, but noticeable, contributions from a d_{z^2} orbital may also be seen in ϕ_1 in the case of Zn^+-Xe, which moves electron density off-axis by means of the "ring" of this orbital. This likely involves the $3d_{z^2}$ orbital, noting that the $3d^9 4s^2$ state is fairly low in energy (see Table 4 and comments on Hg^+-Xe, below). Note that any mixing between the $3d^{10}4s^1$ and $3d^9 4s^2$ states leads to an increased occupancy of the 4s orbital, and so to increased repulsion. Finally, we note a very small amount of π bonding from the RG atom through the highest occupied *n*p orbitals into the Zn^+ dπ orbitals (d_{xz} and d_{yz}).

Similar, although slightly less marked, observations can be made for the MO and contour plots for

Sr^+-RG and Cd^+-RG in Figure 11. On the other hand, for the Ba^+-RG plots in Figure 12, the perturbations are significant. First, we note that the case of Ba^+-He appears to show very little sign of anything except physical interactions. For Ba^+-Ar, however, it is clear that the degeneracies of ϕ_2–ϕ_4 are broken slightly, and that ϕ_8 rises in energy a little compared to Ba^+ 6s, alongside movement in the energy of ϕ_5; these are indicative of minor incipient chemical effects. Most noticeable, however, is the contour of ϕ_8 where quite dramatic off-axis contributions from the low-lying Ba 5d orbitals (Table 4) can be seen, showing that there is significant sd hybridization in these species. Very little further change is seen when moving to Ba^+-Xe.

The implication of the above is that sd hybridization is significant for $M^+ = Ca^+$–Ra^+, but covalency is only a minor effect – it is the lowering of electron density in the internuclear region that is the key driver in these complexes, allowing the RG atom to get close to the M^+ centre and so lower the energy, predominantly via the $-\alpha/2R^4$ term.

Considering now Hg^+-RG, again Hg^+-He shows little indication of any covalency, while for Hg^+-Ar and Hg^+-Xe there is a loss in degeneracy of both the Hg 5d orbitals (ϕ_2–ϕ_6) and the RG *n*p orbitals (ϕ_7–ϕ_9), together with a small rise in energy of ϕ_{10} compared to Hg^+ 6s, indicating that a small amount of covalency is now present. There are minor perturbations in the ϕ_{10} contour on the side opposite to the incoming RG atom, showing that a very small amount of sp hybridization is occurring – noting the high energy of the Hg^+ excited p orbitals (Table 4). Finally, we note that there is a small, but increased amount of π bonding from the RG atom through its highest occupied *n*p orbitals into the Hg^+ dπ orbitals (d_{xz} and d_{yz}). In addition, there is a small amount of mixing between the $5d_{z^2}$ orbital and the RG np_z orbital.

Summary

The overall picture is that the M^+-RG complexes involving Group 12 cations, Be^+ and Mg^+ demonstrate a significant amount of covalency, while those involving Ca^+–Ra^+ show significant sd hybridization, which clearly has a major impact on the interactions via the lowering of electron density in the internuclear region, and can occur when the excited d orbitals lie low in energy. Conversely, the amount of sp hybridization that can occur appears to be small, owing to the high energy of the excited p orbitals in all cases (see Table 4). In fact, the lowest unoccupied (*n*+1)p orbital on Ca^+–Ra^+ is actually lower in energy than those for Be^+ and Mg^+. Hence, some sp as well as sd hybridization is possible in the Ca^+–Ra^+ species, but the latter is by far the most pronounced.

The observed covalency is largely driven by the small radii of these ions, particularly for Be^+; this also occurs for the Group 12 cations, whose smaller cationic radii arise following the traversing of the period,

which leads to orbital contraction. The ability for the RG atom to approach M^+ closely drives the lowering of energy via the $-\alpha/2R^4$ ion/induced-dipole term.

In addition, part of the explanation for the covalency lies with the closer energetic proximity of the outermost M^+ *n*s orbitals to the coulombically-lowered outermost p orbitals on RG. We have just noted that the sd hybridization that arises for Group 2 Ca^+–Ra^+ occurs from the low-lying unoccupied d orbitals (see Table 4), so that the energetic cost of hybridization is small. This is not possible for the other species owing to the much higher-lying unoccupied d orbitals. In such cases, sp hybridization is a possibility, but the unoccupied (*n*+1)p orbitals (Table 4) are relatively high in energy. Indeed, the outermost *n*p orbitals for Group 12 are significantly higher than both the lowest unoccupied *n*d and (*n*+1)p orbitals for Group 2, perhaps explaining why the amount of hybridization is small in these species: i.e. even the rise in the attractive terms from the smaller ionic radii (and so smaller R_e values) of these species cannot overcome the high energetic cost of hybridization.

We also note that in Hg^+-Ar and Hg^+-Xe there are small amounts of $5d_{z^2}$, $5d_{xz}$ and $5d_{yz}$ character mixing with the RG *n*p orbitals; this likely arises from the presence of the excited $5d^96s^2$ state (see Table 4), and causes a loss in degeneracy of the 5d orbitals. The high energy of the excited …$5d^{10}6s^06d^1$ states (see Table 4) means that sd hybridization is unlikely.

We finish by noting that although the Group 2 cations are larger than their neighbouring Group 1 species,[64] actually the corresponding R_e values for M^+-RG involving the Group 2 cations and RG = Ne–Rn are smaller than those involving Group 1[1,2,3,4,5] demonstrating the significant distortions that occur in the former; this also leads to the D_e values from the Group 2 species being the larger. In contrast, the R_e ordering is reversed in the cases of RG = He, demonstrating that deriving R_e values from the M^+-He complexes demonstrate a more intuitive set of ionic radii.[64]

E. Partial Atomic Charge Analyses

Partial atomic charges for the M^+-RG complexes have been calculated using Mulliken, NPA and AIM analyses, and the results are collected in Tables 5 and 6 for the Group 2 and Group 12 complexes, respectively. We initially consider the Group 12 species and then move onto Group 2.

Group 12

There is good agreement between all three methodologies for M^+ = Zn^+–Hg^+. This is somewhat surprising since Mulliken charges are very frequently unreliable. Importantly, all sets of results give the same trend of increasing partial charge on the rare gas atom with its increasing atomic number.

Calculated charges show there is some slight migration of charge taking place in the Ar complexes, in line with the delocalization of orbital density (via covalency) in the φ_7 and φ_{10} orbital contours (see

Figure 10). The amount increases as the RG atomic number increases, but the transfer is slightly smaller for Cd^+ than it is for Zn^+ and Hg^+; for the species containing the lighter RG atoms the values for the latter two metals are very similar, but for RG = Xe and Rn, the amount of charge transfer is slightly larger for Hg^+ (~0.3*e*) than for Zn^+ (~0.2*e*). All of the latter are in line with the atomic radii discussed above. These amounts of charge transfer are quite significant and suggest chemical interactions, in line with the contour plots, the loss in degeneracy of the RG *n*p orbitals and the rise in energy of the M^+ *n*s orbital. The trend also follows the energy of the singly-occupied *n*s orbital (which is energetically the lowest for Hg^+ compared to the other Group 12 M^+ ions).

Group 2

Although in agreement for the lightest two RG atoms, the results from the different methods of charge analysis for Group 2 are in poor agreement with each other and are the most divergent when the atomic numbers of M^+ and RG differ the most, being the poorest for Be^+-Xe and Be^+-Rn. These are the cases when RG is closest to the M^+ centre, and hence it becomes more difficult to decide on which centre the electron density is located. Qualitatively, it seems NPA does the best when compared to the contour plots. For example, the contours for Be^+-Xe suggest a reasonable amount of charge transfer, while for Mg^+-Xe, very little. This seems to correspond best to the NPA charges, since AIM suggests very little transfer, particularly for Mg^+-Xe. Clearly the very large amounts of transfer suggested by the Mulliken analysis are far from reasonable, particularly for Be^+-Rn where the transfer is implied to be > 0.5*e* – we experienced similar issues in recent work on C^+-RG.[66]

Thus, it seems that describing the partial atomic charges for the Group 2 M^+–RG complexes is rather more challenging than for the Group 12 ones, especially so for the Be^+-RG and Mg^+-RG complexes involving the heavier rare gases.

F. Model Potential

In Ref. 18 a model potential was set up and used to investigate chemical versus physical interactions in M^+-RG, mostly based on available experimental data. The model potential employed electrostatic terms up to $1/R^8$ and a two-parameter Born-Mayer potential, and is given in Eq. 2 This idea was extended in Refs. 1 and 6 to include the effect of damping factors,[67] which are given in Eq. 3, which model the attenuation of the different interaction terms at short *R* as a result of overlapping electron densities. Separate damping factors are applied to each $1/R^n$ term in the model, calculated for that value of *n*; note that it is assumed that the *b* parameter in the damping factors is the same as the Born-Mayer *b* parameter. Equations involving the model potential are solved, using values for R_e, D_e and ω_e (see Refs. 1, 6 and 18). This yields the two Born-Mayer potential parameters, *A* and *b* as well as the effective charge on the metal cation, *Z*. The latter is the charge required for the model potential to fit the R_e, D_e and ω_e values; in the case of the physical model being a good description, *Z* should come out to be 1.00. For

the Group 1 M^+-RG complexes studied in Refs. 1 and 6, very little difference between the damped and undamped values were seen, suggesting that there is little interpenetration of the M^+ and RG electron clouds in these species, and so physical interactions dominate.

$$V(R) = -\frac{\alpha_{RG_d} Z^2}{2R^4} - \frac{C_6}{R^6} - \frac{\alpha_{RG_q} Z^2}{2R^6} + \frac{B_{RG} Z^3}{2R^7} - \frac{C_8}{R^8} - \frac{\alpha_{RG_o} Z^3}{2R^8} - \frac{\gamma Z^4}{24R^8} + Ae^{-bR} \tag{2}$$

$$f_n(R) = 1 - \exp(-bR) \sum_{k=0}^{n} \frac{[bR]^k}{k!} \tag{3}$$

In Equation (2) and Table 7, the α terms, denoted in an obvious way, are the dipolar, quadrupolar and octupolar polarizabilities of the RG atoms, C_6 and C_8 are the usual dispersion coefficients (calculated from the polarizabilities of RG and M^+ using the Slater-Kirkwood[68] and Koutselos and Mason[69] approximations), N is the effective number of "oscillator" electrons used to calculate C_6 and C_8,[68] B is the dipolar-quadrupolar polarizability of RG, and γ is the hyperpolarizability of RG; A and b are the Born-Mayer parameters. In Table 7 we present the values for these quantities used in the present work, many of which are well-established, or have been calculated or estimated – see Ref. 18. We have employed the values from that work, with the following exceptions. The α_d values for Sr^+, Ba^+ and Ra^+ were taken from Ref. 70, while α_q for Sr^+ was taken from Ref. 71 (the same source for this quantity as the other Group 2 cations up to Ba^+), and α_q for Ra^+ was taken from Ref. 72. Values of N for Sr^+, Ra^+ and Rn were estimated in the present work. For Rn, values of α_d and γ were taken from Ref. 73, while values for α_q, α_o and B were estimated herein. In the top part of Table 8 we show the calculated charges for the Group 2 M^+-RG complexes. It is notable that, except for the cases of Be^+-RG, for all complexes involving RG = He and Ne, the calculated charges are between 0.97 and 1.25, either damped or undamped. We also note that in most cases damping leads only to the expected small increase in the calculated effective charge. For Be^+-RG, the damped effective charge is calculated to be significantly larger, and in the notable case of Be^+-Ne, the damped value is 1.43, while the undamped one is 0.97. This may be indicative of significant penetration of the electron clouds, but the MO plots in Figure 9 suggest otherwise; more likely is that this is caused by the simplicity of the model potential, and hence spurious values of Z arise when the potential is not working well. In the above, we have noted the high degree of covalency in the Be^+-RG complexes, and the unusual reduced potential plots for the Group 2 M^+-Ne complexes; later we shall emphasise that Be^+-Ne is a very unusual case.

We see that the charges for the M^+-Ar complexes have surprisingly low calculated Z values, as does Ba^+-Kr. Peculiarly, although solutions to the undamped model potential equations were obtained for

Ba^+-Ar in Ref. 18, no solutions were possible here, either damped or undamped, using the calculated R_e, D_e and ω_e values for this species. Again, this points to the interactions being somewhat unusual for this complex. Solution to the model potential equations makes use of two parameters that are representative of the minimum (R_e and ω_e), as well as D_e; furthermore, it is assumed that the electrostatic and Born-Mayer parameters are applicable to the whole potential – indeed, in Ref. 6 we were able to show that the model potential with the obtained *Z*, *A* and *b* parameters fitted the whole calculated potential very well for the lightest, Li^+-He, and the heaviest, Cs^+-Xe, Group 1 complexes considered. In those cases, *Z* had a value very close to 1.00, demonstrating that the interactions in those species were largely physical in nature. The suggestion from the values in Table 8 is that this is not the case for many of these species.

In summary, when significant amounts of *R*-dependent changes in the amount of hybridization occur, such as in the Group 2 M^+-RG complexes, then trying to model the interaction with a simple model potential such as Eq. 2 becomes futile. It is notable that the model potential fails completely for Ba^+-Ar in that no solution for *Z* could be found.

For the Group 12 species, whose calculated *Z* values are presented in the bottom part of Table 8, we find largely that the model potential solutions give rise to *Z* values in the range 0.95–1.15 for most of the species, with generally a small increase when damping is included, and hence it appears to be working well. That slightly larger values are calculated for the heaviest Hg^+-RG complexes, suggests that those values may be fortuitously "sensible" and that in fact the model potential is not appropriate. This would be in line with the significant amounts of covalency observed in the contour plots, discussed above, which would also be *R* dependent.

G. Birge-Sponer Plots

In general, close to R_e, one would expect a diatomic species to be described well by a linear Birge-Sponer plot and then at long-range this would transfer over into Leroy-Bernstein behaviour.[74,75,76] For a suitably high number of bound levels, this long-range behaviour is expected to follow a $(\Delta G_{v+1/2})^{2n/(n+2)}$ dependence, where *n* is that of the R^{-n} dependence of the potential at long range. For an atomic cation/rare gas interaction, an R^{-4} dependence is expected, and so we expect a $(\Delta G_{v+1/2})^{4/3}$ dependence at long range. Hence, we expect the Birge-Sponer plots for the M^+-RG complexes to be approximately linear, but then to deviate, exhibiting a $(\Delta G_{v+1/2})^{4/3}$ dependence for high *v*, i.e. close to the dissociation limit.

In Figures 13–16 we present plots of $\Delta G_{v+1/2}$ *vs.* $(v+1)$ for the Group 2 and Group 12 M^+–RG complexes where *v* is the value for the lower of a pair of consecutive vibrational levels; although not strictly a Birge-Sponer plot (where the abscissa would be $v+1/2$), we use the term here for convenience. On each graph, the red points correspond to the calculated spacings between adjacent calculated vibrational

levels, while the solid black "Morse line" corresponds to "Morse spacings" calculated from the vibrational constants ω_e and $\omega_e x_e$ presented in Tables 1 and 2; as noted above, derivation of the constants ω_e and $\omega_e x_e$ relies on only the lowest two vibrational levels together with the D_e value. Hence, the correspondence between the red points and the black line gives an indication of how consistent the curvature close to R_e is with regard to the shape of the rest of the IEC. We see that these plots give much more information than simply the values of D_e^{Morse}/D_e presented in Tables 1 and 2; in particular, in many cases they exhibit evidence for changes in the curvature of the IEC from R_e to the dissociation asymptote. So, for example, D_e^{Morse}/D_e for Mg^+-Ne is 1.05 and it might be expected that the Morse line would largely agree with the Birge-Sponer one for this complex; however, the plot shows that the Birge-Sponer plot is in fact curved with some vibrational levels falling below the Morse line while others lie above. Overall these deviations largely cancel out across the whole of the plot, so that the D_e^{Morse}/D_e value hides the fact that these variations in the shape of the IEC are occurring. It is clear, therefore, that caution is merited in deducing too much from the D_e^{Morse}/D_e ratios in Tables 1 and 2. However, it is clear that when values are far from 1.00, either below or above, then it is likely that the BS plot will show non-standard behaviour.

If we examine the BS plots for Be^+-RG in Figure 13, we see that for RG = Ar and Kr, the behaviour is much as expected, with the linear region at low *v* following the Morse line closely, and the LeRoy-Bernstein deviation for the higher values. However, for RG = Xe and Rn the BS plot has dipped under the Morse line for intermediate values of *v*; we interpret this in terms of a change in the interaction terms at long- versus short-*R*. As covalency and small amounts of sp hybridization occur, the attractive and repulsive parts of the potential will change, leading to curvature in the BS plot. The effect is most stark in the case of Be^+-Ne, where the BS points lie far under the Morse line, indicating that the curvature of the IEC close to R_e is very different from that at even moderate *R* values. One can visualize this most easily by considering the Be^+ and Ne atoms approaching each other from long range, as Ne gets closer, attracted by the positive charge, its electrons start to interact with the Be^+ 2s one and this brings in a repulsive term. This softens the potential at moderate *R* values (being the sum of the attractive and repulsive terms), and so causes the decrease in slope of the BS plot for low *v*. (Recall that the Be^+-Ne reduced potential plot in Figure 3 showed the starkest deviation from the behaviour of the other Be^+-RG species, indicating a greater role of the repulsive potential.) It may thus be seen that Be^+-Ar and Be^+-Kr are intermediate cases where the sum of the attractive and repulsive terms gives approximately linear BS plots and Morse-like behaviour. (Note that little can be said regarding the plot for Be^+-He, since there are so few bound levels.) A very similar picture can be seen for the Mg^+-RG complexes, although Mg^+-Ne does not show the stark deviation from the Morse line seen for Be^+-Ne (again in line with the reduced potential plots in Figure 3). We rationalize this by the fact that Mg^+ is larger than Be^+ owing to the better shielding in the former, this leads to less overlap of the Ne and Mg^+ 3s orbitals than the corresponding situation in Be^+-Ne.

When we examine the BS plots for Ca^+-RG – Ra^+-RG in Figures 14–16, we see that these show unusual shapes, most noticeably in the RG = Ar–Xe plots. There is the expected long-range curved region, but then an approximately linear section at mid-v values and then a steepening of the potential at low-v. This changing slope is likely attributable to the sd hybridization (see molecular orbital plots and above discussion) that will lead to an R-dependent change in the form of the potential as the RG atom approaches M^+, giving rise to very un-Morse-like behaviour as the electron density moves off-axis. Close to R_e, however, we assume that the amount of electron density in the sd hybrid orbitals reaches a level whereby repulsion effects come into play, and this causes a steepening of the potential in this region. As with Be^+-Ne, this steepening is not seen for RG = Ne, since it is not polarizable enough to offset the cost of hybridizing enough of the electron density for this to occur.

We now examine the Group 12 M^+-RG BS plots in Figures 14–16. We see that for Zn^+-RG, Figure 14, there is a close-to-linear region for low v, but some bowing occurs for Zn^+-Xe and this is more noticeable for Zn^+-Rn. Matching this with the MO diagrams in Figure 10, we can see that there is a minor amount of elongation of the Zn^+ 4s orbital on the side opposite to the incoming RG atom, and this is in line with only minimal sp hybridization because of the high 4p ← 4s excitation energy (Table 4). Instead, energy is gained by some covalency with electron density transferred into the outermost np orbital on the RG atom. However, in the high-v region, far from R_e, a significant amount of repulsion occurs as the incoming RG atom gets cushioned by the 4s electron density, causing an overall softening of the potential, such as in Zn^+-Xe, and hence the curvature of the BS plot into a lower-gradient region; however, for the low-v region, close to R_e, the curve steepens again to the "standard" behaviour. Note that it is difficult to discern these effects in either the IECs or reduced potential plots in Figures 2 and 4. A similar picture appears to hold for the Cd^+-RG BS plots, Figure 15, but with the bowing being slightly less pronounced, likely caused by the slightly larger Cd^+ ion; this is also consistent with the smaller amount of outermost np contribution to the MOs in the plots – see Figure 11. When we move on to examining the BS plots for Hg^+-RG in Figure 16, however, it may be seen that there is significant departure from the Morse line, and significant bowing of the BS plot from mid- to low-v. Again, by examining the MO contour plots in Figure 12, the amount of sp hybridization appears to be small, as no elongation of the Hg^+ 6s orbital is noticeable; however, there is prominent mixing of the Hg^+ 6s and outermost $n\mathrm{p}_z$ RG orbitals at R_e. Furthermore, although there are small contributions in the cases of Zn^+-RG and Cd^+-RG, in Hg^+-RG a sizeable mixing between the $n\mathrm{p}_{x,y}$ RG orbitals and the d_{xz} and d_{yz} orbitals is evident. The MO contour plots in Figure 12 suggests that these d orbitals are (n-1)d orbitals, and there is a distinct break in the degeneracy in the five 5d orbitals in the Hg^+-Ar and Hg^+-Xe plots in Figure 12. It is interesting to note the contrast between the MO contour plots of Ba^+-RG and Hg^+-RG in Figure 12 (and, to a lesser extent the corresponding comparisons in Figures 10 and 11). The sd hybridization dominates in the case of the Group 2 species (Ca^+-RG – Ra^+-RG), but this is minimal for the corresponding Group 12 species because the available d orbitals for hybridization are so much

higher in energy (Table 4). In the case of Hg^+-RG, where the $5d^96s^2$ "d-hole" state is relatively low in energy (but still far higher than the nd^1 states for Group 2), hybridization does not occur to any great extent since this would lead to higher electron density in the Hg^+ 6s orbital, enhancing rather than alleviating the electron repulsion. In addition, the *n*p orbitals are also significantly higher in energy for the Group 12 species, and this means that sp hybridization is too costly to contribute much to the stabilization of these species. Hence, the only route open is small amounts of covalency/charge transfer.

H. *H*(*R*) values

In Table 9 we present the values of the *H*(*R*) parameter from the AIM analysis. It has been argued that a robust criterion for determining covalency is that the total local electronic energy density, *H*(*R*), has a negative value.[77] The values of the *H*(*R*) parameter imply that there is a small amount of covalency for all of the Be^+-RG complexes except for RG = He, and that the amount of covalency increases with the atomic number of RG. For Mg^+-RG there are only small indications of covalency for the heavier species. Overall, this appears to be in line with the MO contour plots in Figure 9, with the covalency enhanced for Be^+-RG because of the smaller size of Be^+, allowing the RG atoms to approach more closely. Of the series that exhibit covalency, the Mg^+-RG complexes are the most weakly bound. This can be attributed to the larger size of the Mg^+ ion coupled with its 3s orbital being furthest from the outermost RG *n*p orbitals energetically. When we then look at the *H*(*R*) values for the other Group 2 M^+-RG complexes for $M^+ = Ca^+–Ra^+$, we see that these values are all positive indicating essentially no covalency; the implication is that the observed sd hybridization on the metal centre occurs as a result of the incoming RG atom, but the effects are all atom-centred and lead to minimal sharing of electron density between M^+ and RG – see MO diagrams, contour plots and above discussion.

For the Group 12 species, there is no covalency for the species with RG = He and Ne. However, all of the other M^+-RG complexes have $H(R) < 0$ (except for Cd^+-Ar), and the magnitude increases with the atomic number of RG. The Cd^+-RG series has the smallest covalency, which is again in line with the larger size of Cd^+. These covalency effects are reflected in the equilibrium dissociation energies of the Group 12 complexes, which are much higher than for the corresponding M = Ca–Ba complexes with the heavier rare gases, and more in line with the M = Be and Mg complexes. The Be^+-RG series is the most strongly bound out of both Groups 2 and 12, owing to the small size of Be^+ and its low number of electrons. These comments are in line with the MO diagrams, contour plots and above discussion.

4. CONCLUSIONS

In the present work we have reported high-quality IECs for M^+-RG complexes for RG = He–Rn and $M^+ = Be^+–Ra^+$ and $Zn^+–Hg^+$. These were calculated at the RCCSD(T) level of theory, and were basis set extrapolated from quadruple- and quintuple-ζ basis sets. From these IECs we have calculated R_e values and spectroscopic constants, which are in excellent agreement with the small number of

experimental values available. Further, trends in some of the key constants have been examined, which indicated that the interactions across these species were different.

We hence examined the interactions in the Group 2 and Group 12 M^+-RG complexes using a range of approaches. One of the key indicators was the MO diagrams combined with the MO contour plots. These indicated that even though both of these series of metals have …*n*s^1 electronic configurations, there are three modes of interaction: physical, covalent and sd hybridization, with the latter alleviating the repulsion that occurs as the electrons on the approaching RG atom start to interact with the outermost *n*s orbital on M^+. The role of covalency was confirmed by an examination of the AIM $H(R)$ parameter, which concurred that this was present for Be^+-RG (RG = Ne–Rn), minimally present for Mg^+-RG (RG = Kr–Rn), and present for all Group 12 M^+-RG species for RG = Ar–Rn (except for Cd^+-Ar). For Be^+-He, Mg^+-RG (Rg = He–Ar), covalency was largely non-existent, and although also absent for the complexes with $M^+ = Ca^+$–Ra^+ and RG = Ar–Rn, there was significant sd hybridization in those cases to facilitate the interaction.

Hence for Be^+-He, Mg^+-RG (RG = He–Ar), the Group 12 M^+-RG (RG = He and Ne) and Cd^+-Ar complexes, we conclude that the interactions are "physical", with no clear evidence of chemical behaviour. For Be^+-RG (RG = Ne–Rn), Mg^+-RG (RG = Kr–Rn) and the Group 12 M^+-RG complexes (RG = Ar–Rn, but not Cd^+-Ar), we conclude that the interactions have a covalent contribution, which varies, but is most prominent for the species with the heavier RG atoms. Finally, for the Group 2 M^+-RG complexes ($M^+ = Cd^+ – Ra^+$, RG = Ar–Rn), there are no indications of covalency, since $H(R) > 0$, but consistent with comments made in some of our earlier work,[9,10] we describe the significant sd hybridization as chemical as it involves a significant perturbation of electron density that results in a stronger interaction. In contrast to comments made in some of our earlier work, sp hybridization appears to be minimal and covalency is the main mode of interaction for $M^+ = Be^+$ and Mg^+ for RG = Ar–Rn.

We believe that sd hybridization (and to a much lesser extent, sp hybridization) causes a breakdown in the model electrostatic potential (Eq. 2). This occurs since the potential uses fixed values for a range of electrostatic quantities applicable to a particular electronic state of M^+, and so they have no R dependence; however, the sd hybridization is R dependent and happens to differing extents. Thus, we see from Table 8 that for the cases where the heavier Group 2 M^+ are interacting with the heavier RG, values very far from the "physical" value of 1.00 are observed, with no solution being found for Ba^+-Ar. The failure of the model potential is particularly marked for the Ba^+-RG complexes owing to the very low energy of the unoccupied 5d orbitals; indeed, barium has been suggested as being an honorary transition metal.[78,79] In contrast, except for Be^+-Ne (see below), we find Z values fairly close to 1.00 for the Be^+-RG, Mg^+-RG and most of the Group 12 M^+-RG complexes; however, given the covalency deduced for these species, these "sensible" values may simply be fortuitous, and the extent of covalency will be R dependent.

The model potential results for Be^+-RG are unusual. As can be seen from Table 8, for most species, there is at most a very small rise in Z when damping is included, as expected – this is even true for the heavier Group 2 M^+-RG complexes, where sd hybridization causes the model to fail. However, for the Be^+-RG complexes, the rises are quite substantial for all except Be^+-He, and is particularly marked for Be^+-Ne. We note that the BS plot in Figure 13 for this complex is also very unusual, and suggests that repulsion is playing a major role at R_e. Indeed, the value of the derived repulsive potential at R_e is 5.6×10^{-3} E_h for the undamped potential and 1.90×10^{-3} E_h for the damped potential. This, and the values for the other Be^+-RG potentials, suggests that the simple electrostatic model potential with a two-parameter Born-Mayer potential is not sufficient to describe a potential where the RG and M^+ orbitals overlap and the attractive and repulsive terms are R-dependent.

A number of observations in the present work suggest that creating a universal diatomic potential would be extremely difficult, particularly the observation of R-dependent hybridization, covalency and repulsion. These also suggest that defining a radius for an atom or atomic cation that is transferable to a wide range of species is also fraught with danger, as the interactions can be so different.

Supporting Information

PECs for all of the M^+-RG systems discussed in the present work are provided as supplementary material. The presented PECS are calculated at the RCCSD(T) level and after basis set extrapolation (see main text for details of the basis sets employed).

Acknowledgements

We thank the University of Nottingham for studentship to W.D.T and the EPSRC (EP/I012303/1) for a studentship to J.P.H. Calculations were performed on the High Performance Computer facility at the University of Nottingham.

Table 1: Spectroscopic constants for the Group 2 M^+-RG series.[a,b]

	R_e / Å	D_e / cm^{-1}	D_0 / cm^{-1}	ω_e / cm^{-1}	$\omega_e x_e$ / cm^{-1}	B_e / cm^{-1}	α / cm^{-1}	k / N m^{-1}	D_e^{Morse} / D_e
Be^+-He	**2.922** 2.924	**133** 133	**98** 98	**76.8** 76.3	**11.8** 11.7	**0.724** 0.723	**0.1420** 0.142	**0.96** 0.950	**0.94** 0.94
Be^+-Ne	**2.437** **2.452** 2.454 (2.462)	**424** **407** 407 (404)	**391** **375** 375 (372)	**67.4** **64.5** 65.2 (65.6)	**1.16** **1.06** 1.47 (1.63)	**0.463** **0.456** 0.456 (0.453)	**0.0055** **0.0064** 0.00607	**1.66** **1.52** 1.56	**2.31** **2.42** 1.78
Be^+-Ar	**2.086** **2.086** 2.084 *2.0855(6)*[c]	**4405** **4401** 4428	**4226** **4221** 4248 *3933(200)*[c]	**363.0** **363.1** 364.1 *362.7(1)*[c]	**9.02** **9.03** 8.94 *8.92(5)*[c]	**0.527** **0.527** 0.528 *0.5271(3)*[c]	**0.0148** **0.0148** 0.0147 *0.0145(3)*[c]	**57.11** **57.13** 57.4	**0.83** **0.83** 0.84
Be^+-Kr	**2.217** 2.221 *2.2201*	**6072** 6053	**5891** 5872	**366.0** 365.5 *367.14*[d]	**5.90** 5.82 *6.21*[d]	**0.421** 0.420 *0.42030*[d]	**0.0082** 0.00816 *0.00821*[d]	**64.25** 64.0	**0.94** 0.95
Be^+-Xe	**2.403** 2.407	**8273** 8239	**8087** 8054	**373.7** 372.8 *~367*[e]	**4.10** 4.04 *~3.7*[e]	**0.346** 0.345	**0.0049** 0.00486	**69.42** 69.0	**1.03** 1.04
Be^+-Rn	**2.482** 2.486	**9485** 9491	**9300** 9306	**371.7** 371.0	**3.43** 3.32	**0.316** 0.315	**0.0038** 0.00381	**70.5** 70.1	**1.06** 1.10
Mg^+-He	**3.481** 3.482	**73** 73	**51** 52	**47.4** 45.8	**8.50** 7.68	**0.413** 0.412	**0.0909** 0.0900	**0.45** 0.424	**0.91** 0.95
Mg^+-Ne	**3.119** **3.147** 3.145 *3.17(5)*[f]	**206** **203** 203	**185** **182** 182 *96(50)*[f]	**43.5** **42.7** 43.1 *41*[f]	**2.39** **2.28** 2.44	**0.159** **0.156** 0.157	**0.0103** **0.0098** 0.00987	**1.22** **1.17** 1.19	**0.96** **0.99** 0.94
Mg^+-Ar	**2.825** **2.825** 2.822 *2.825(7)*[g]	**1291** **1290** 1299	**1240** **1238** 1247 *1210(165)*[g]	**104.5** **104.7** 104.8 *96*[g]	**2.70** **2.68** 2.53	**0.141** **0.141** 0.141	**0.0041** **0.0041** 0.00407	**9.65** **9.69** 9.71	**0.78** **0.79** 0.84
Mg^+-Kr	**2.875** 2.884	**2001** 1978	**1942** 1919 *1800(600)*[g]	**119.6** 118.4 *112*[g]	**2.14** 2.08	**0.109** 0.109	**0.0021** 0.00213	**15.7** 15.4	**0.84** 0.85
Mg^+-Xe	**3.010** 3.018	**3012** 2973	**2944** 2906 *3300(1700)*[g]	**135.9** 134.8	**1.57** 1.66	**0.092** 0.0912	**0.0012** 0.00123	**22.1** 21.7	**0.98** 0.92
Mg^+-Rn	**3.057** 3.064	**3666** 3639	**3595** 3569	**142.1** 141.1	**1.41** 1.41	**0.083** 0.0830	**0.0009** 0.000919	**25.7** 25.4	**0.97** 0.97
Ca^+-He	**4.240** 4.259	**37** 36	**24** 23	**28.8** 25.6	**6.16** 4.88	**0.264** 0.264	**0.0698** 0.00730	**0.18** 0.141	**0.91** 0.93
Ca^+-Ne	**3.744** 3.760 *3.70(5)*[j]	**111** 109 *115(5)*[j]	**100** 97 *103(5)*[j]	**23.2** 24.8 *26(2)*[j]	**1.10** 1.50	**0.091** 0.0889	**0.0050** 0.00591	**0.42** 0.484	**1.10** 0.94
Ca^+-Ar	**3.108** 3.256 *3.20(0.15)*[k]	**877** 742 *810(60)*[k]	**841** 712	**72.5** 60.6 *69(2)*[k]	**2.43** 1.59	**0.087** 0.0795	**0.0029** 0.00255	**6.19** 4.33	**0.62** 0.78
Ca^+-Kr	**3.174** 3.305 *3.30(0.15)*[l]	**1376** 1200 *1280(80)*[l]	**1336** 1160	**79.6** 69.7 *77(2)*[l]	**1.70** 1.31	**0.062** 0.0570	**0.0013** 0.00116	**10.12** 7.76	**0.68** 0.78
Ca^+-Xe	**3.330** 3.457	**2034** 1780	**1991** 1740	**87.1** 78.2	**1.17** 1.03	**0.050** 0.0460	**0.0007** 0.00064	**13.72** 11.1	**0.80** 0.83

	3.45(0.15)[m]	*1850(100)*[m]	*1811(80)*[m]	*84(2)*[m]					
Ca^+-Rn	**3.378** 3.487	**2493** 2190	**2448** 2150	**89.9** 81.9	**0.96** 0.88	**0.044** 0.0410	**0.0005** 0.00046	**16.1** 13.4	**0.85** 0.87
Sr^+-He	**4.524** 4.547	**30** 29	**19** 19	**24.4** 21.1	**5.49** 4.12	**0.221** 0.220	**0.0609** 0.0652	**0.13** 0.10	**0.90** 0.94
Sr^+-Ne	**3.979** 4.005	**93** 91 *77*[n]	**84** 82 *67/85*[n]	**18.0** 19.5 *19.5(1.5)*[n]	**0.73** 1.11 *1.12(0.5)*[n]	**0.066** 0.0650	**0.0032** 0.00398	**0.31** 0.37	**1.20** 0.94
Sr^+-Ar	**3.327** 3.385	**712** 646 *830(240)*[o]	**685** 623 *800(240)*[o]	**54.3** 47.3 *49.5*[o]	**1.89** 1.21 *0.75*[o]	**0.056** 0.0535	**0.0017** 0.00162	**4.77** 3.63	**0.55** 0.72
Sr^+-Kr	**3.385** 3.433	**1120** 1050 *1231*[p]	**1092** 1030 *1200(580)*[p]	**55.1** 51.1 *52(1)*[p]	**1.03** 0.85 *0.6*[p]	**0.034** 0.0333	**0.0006** 0.000578	**7.67** 6.62	**0.66** 0.73
Sr^+-Xe	**3.535** 3.591	**1660** 1560 *1970(440)*[q]	**1631** 1530	**58.3** 54.7 *54.6*[q]	**0.62** 0.60 *0.38*[q]	**0.026** 0.0248	**0.0003** 0.000278	**10.56** 9.32	**0.83** 0.80
Sr^+-Rn	**3.576** 3.617	**2052** 1910	**2023** 1910	**58.4** 55.4	**0.48** 0.47	**0.021** 0.0205	**0.0002** 0.000177	**12.65** 11.4	**0.86** 0.84
Ba^+-He	**4.912** 4.950 [4.921][r] {4.917}[r]	**23** 22 [22][r] {23}[r]	**14** 13 [14][r] {14}[r]	**19.6** 16.7 [17.0][r] {17.2}[r]	**4.65** 3.39 [3.45][r] {3.99}[r]	**0.185** 0.183	**0.0545** 0.0555	**0.09** 0.064	**0.91** 0.95
Ba^+-Ne	**4.249** 4.291 [4.267][r] {4.246}[r]	**76** 73 [75][r] {77}[r]	**69** 65 [68][r] {69}[r]	**14.6** 15.1 [15.4][r] {15.6}[r]	**0.64** 0.82 [0.92][r] {0.90}[r]	**0.054** 0.0529	**0.0018** 0.00291	**0.22** 0.24	**1.10** 0.95
Ba^+-Ar	**3.319** 3.385 *3.364*[s] *3.47*[t] [3.339][r] {3.348}[r]	**811** 693 *680*[s] *~800*[t] [766][r] {752}[r]	**778** 664 [734][r] {720}[r]	**67.8** 58.6 *61.7(1.5)*[s] [65.6][r] {63.9}[r]	**2.24** 2.19 *2.3(0.2)*[s] [2.80][r] {2.72}[r]	**0.049** 0.0476	**0.0013** 0.00147 *0.00125*[r]	**8.38** 6.27	**0.63** 0.57
Ba^+-Kr	**3.415** 3.479 [3.438][r] {3.446}[r]	**1215** 1093 [1175][r] {1164}[r]	**1186** 1066 [1147][r] {1136}[r]	**59.3** 53.9 [57.8][r] {56.9}[r]	**0.97** 1.02 [1.14][r] {1.12}[r]	**0.028** 0.0267	**0.0004** 0.000428	**10.83** 8.92	**0.75** 0.65
Ba^+-Xe	**3.581** 3.653 [3.612][r] {3.621}[r]	**1731** 1569 [1672][r] {1663}[r]	**1703** 1543 [1645][r] [1636][r]	**56.2** 52.3 [55.3][r] [54.6][r]	**0.18** 0.61 [0.65][r] {0.63}[r]	**0.020** 0.0187	**0.0002** 0.000192	**12.52** 10.87	**2.57** 0.71
Ba^+-Rn	**3.635** 3.709	**2100** 1916	**2073** 1892	**53.5** 49.5	**0.45** 0.41	**0.015** 0.0144	**0.0001** 0.00011	**14.36** 12.31	**0.76** 0.79
Ra^+-He	**4.871** 4.885	**24** 23	**15** 15	**20.3** 17.6	**4.79** 3.55	**0.186** 0.186	**0.0536** 0.0553	**0.10** 0.07	**0.90** 0.94
Ra^+-Ne	**4.268** 4.276	**79** 77	**71** 69	**16.2** 16.3	**0.73** 0.92	**0.050** 0.0504	**0.0027** 0.00311	**0.28** 0.29	**1.12** 0.95
Ra^+-Ar	**3.704** 3.759	**526** 486	**507** 469	**37.5** 34.3	**1.14** 0.78	**0.036** 0.0351	**0.0010** 0.000949	**2.82** 2.36	**0.59** 0.78
Ra^+-Kr	**3.735** 3.775	**831** 793	**813** 775	**36.8** 34.9	**0.64** 0.52	**0.020** 0.0193	**0.0003** 0.000294	**4.87** 4.40	**0.64** 0.74
Ra^+-Xe	**3.871** 3.917	**1235** 1170	**1216** 1160	**37.6** 35.9	**0.42** 0.35	**0.014** 0.0132	**0.0001** 0.000127	**6.93** 6.33	**0.68** 0.78
Ra^+-Rn	**3.897** 3.944	**1546** 1470	**1528** 1450	**35.8** 34.6	**0.15** 0.25	**0.010** 0.00967	**0.0001** 0.000069	**8.48** 7.89	**1.34** 0.82

[a] R_e is the equilibrium bond length, D_e and D_0 are the equilibrium and zero point dissociation energies respectively, ω_e is the harmonic vibrational frequency, $\omega_e x_e$ is the anharmonicity constant, B_e the rotational constant, α the vibration-rotation constant, k the force constant from Hooke's law, and D_e^{Morse} is the Morse estimate of the dissociation energy, given by $\omega_e^2/4\omega_e x_e$. The most prevalent naturally-occurring isotope was used in all cases.

[b] A bold value indicates a value from the present work, with a bold, underlined value indicating a value obtained with a doubly-augmented basis set from the present work (see text). A normal value indicates one previously published by us (see text) and a value in italics indicates an experimental value.

[c] Ref. 33. [d] Ref. 34. [e] Ref. 35. [f] R_0 value, Ref. 36. [g] R_0 value, Refs. 37 and 38. [h] Ref. 38. [i] Ref. 38.[j] Ref. 42. [k] Refs. 43, 44, 45 and 46. [l] Refs. 43, 44 and 45. [m] Refs. 43, 44 and 45. [n] Ref. 47. [o] Ref. 48. [p] Ref. 49. [q] Ref. 50. [r] Ref. 56. Values in square brackets are the non-small core ECP/CBS results and values in braces are the non-small core ECP/BF/C5Z results from Ref. 56 (see Table IV in that work). [s] Ref. 51. [t] Ref. 52.

Table 2: Spectroscopic constants for the Group 12 M^+-RG series.[a, b]

	R_e / Å	D_e / cm^{-1}	D_0 / cm^{-1}	ω_e / cm^{-1}	$\omega_e x_e$ / cm^{-1}	B_e / cm^{-1}	α / cm^{-1}	k / Nm^{-1}	D_e^{Morse} / D_e
Zn^+-He	**3.014**	**131**	**99**	**68.8**	**10.01**	**0.498**	**0.0861**	**1.05**	**0.90**
	3.03	125.3	94	63.0	8.36	0.487		0.88	0.95
Zn^+-Ne	**2.807**	**348**	**320**	**58.6**	**2.84**	**0.141**	**0.0075**	**3.09**	**0.87**
	2.86	325.4	298	55.5	2.62	0.135		2.76	0.90
Zn^+-Ar	**2.627**	**2062**	**2002**	**119.7**	**2.04**	**0.099**	**0.0018**	**20.8**	**0.85**
	2.64	1977	1918	120.7	2.14	0.098		21.1	0.86
Zn^+-Kr	**2.656**	**3291**	**3229**	**123.6**	**1.25**	**0.066**	**0.0007**	**32.7**	**0.93**
	2.67	3192	3132	120.3	1.22	0.065		30.9	0.93
Zn^+-Xe	**2.759**	**5197**	**5131**	**132.3**	**0.81**	**0.052**	**0.0004**	**44.4**	**0.93**
	2.77	5088	5023	129.9	0.79	0.051		42.8	1.05
Zn^+-Rn	**2.806**	**6372**	**6307**	**130.9**	**0.68**	**0.043**	**0.0002**	**50.1**	**0.99**
	2.81	6285	6221	128.6	0.60	0.043		48.4	1.10
Cd^+-He	**3.204**	**114**	**85**	**63.2**	**9.88**	**0.429**	**0.0775**	**0.91**	**0.89**
	3.24	108		59.4	8.85	0.415		0.80	0.92
Cd^+-Ne	**3.022**	**297**	**272**	**52.1**	**2.72**	**0.109**	**0.0058**	**2.72**	**0.84**
	3.07	276		48.9	2.47	0.105		2.40	0.88
Cd^+-Ar	**2.914**	**1497**	**1452**	**89.8**	**1.61**	**0.067**	**0.0012**	**14.0**	**0.83**
	2.94	1408		86.5	1.55	0.066		13.0	0.86
Cd^+-Kr	**2.922**	**2390**	**2346**	**89.2**	**0.94**	**0.041**	**0.0004**	**22.6**	**0.88**
	2.96	2260		85.6	0.92	0.040		20.9	0.88
Cd^+-Xe	**2.995**	**3886**	**3838**	**96.3**	**0.60**	**0.031**	**0.0002**	**33.4**	**1.00**
	3.03	3705		93.2	0.60	0.030		31.3	0.98
Cd^+-Rn	**3.025**	**4870**	**4823**	**94.3**	**0.43**	**0.024**	**0.0001**	**39.4**	**1.05**
	3.06	4763		92.0	0.43	0.024		37.5	1.03
Hg^+-He	**3.077**	**149**	**113**	**78.7**	**11.78**	**0.458**	**0.0761**	**1.43**	**0.88**
	3.12	138		71.9	10.30	0.441		1.20	0.91
	3.10	144		74.3	10.55				
Hg^+-Ne	**3.002**	**351**	**322**	**60.3**	**3.09**	**0.103**	**0.0050**	**3.90**	**0.84**
	3.06	316		54.8	2.77	0.099		3.22	0.86
	3.04	334		27.0	2.81				
	2.98(3)[c]	*346*[c]		*57.8(1.0)*[c]					
Hg^+-Ar	**2.876**	**1802**	**1754**	**97.4**	**1.35**	**0.061**	**0.0009**	**18.7**	**0.98**
	2.91	1650		92.9	1.49	0.060		17.0	0.88
	2.90	1720		95.4	1.50				
	2.868[d]	*1630(100)*[d]		*99.0*	*1.5*				
Hg^+-Kr	**2.856**	**3111**	**3062**	**97.1**	**0.85**	**0.035**	**0.0003**	**32.9**	**0.89**
	2.89	3867		92.0	0.80	0.034		29.6	0.68
Hg^+-Xe	**2.905**	**5546**	**5494**	**104.1**	**0.42**	**0.025**	**0.0001**	**50.9**	**1.17**
	2.95	5237		100.7	0.44	0.024		47.7	1.10
Hg^+-Rn	**2.938**	**7140**	**7091**	**98.2**	**0.42**	**0.019**	**0.0001**	**60.1**	**0.80**
	2.98	6997		95.2	0.27	0.018		56.5	1.20

[a] R_e is the equilibrium bond length, D_e and D_0 are the equilibrium and zero point dissociation energies respectively, ω_e is the harmonic vibrational frequency, $\omega_e x_e$ is the anharmonicity constant, B_e the rotational constant, α the vibration-rotation constant, k the force constant from Hooke's law, and D_e^{Morse} is the Morse estimate of the dissociation energy, given by $\omega_e^2/4\omega_e x_e$. The most prevalent naturally-occurring isotope was used in all cases.

[b] A bold value indicates a value from the present work, with a bold, underlined value indicating a value obtained with a doubly-augmented basis set from the present work (see text). A normal value indicates one previously published by us (see text) and a value in italics indicates an experimental value.

Table 3: κ values (see Eq. 1) for the Group 2 and Group 12 M^+-RG Complexes

M	M^+-He	M^+-Ne	M^+-Ar	M^+-Kr	M^+-Xe	M^+-Rn
Group 2						
Be	31.1	11.7	28.4	26.2	24.4	23.1
Mg	38.0	29.3	30.0	32.7	33.4	33.0
Ca	43.3	26.7	34.3	37.3	37.4	37.1
Sr	46.0	26.7	37.3	39.5	40.0	39.7
Ba	47.1	26.2	57.3	52.3	46.7	45.5
Ra	48.0	32.8	37.0	41.2	42.4	41.9
Group 12						
Zn	36.6	35.1	35.0	35.2	32.8	31.2
Cd	41.3	41.4	40.1	40.7	38.8	37.3
Hg	45.8	50.4	43.1	43.5	39.0	36.6

Table 4: Energies (cm^{-1}) of the excited s^0p^1, d^9s^2 and s^0d^1 states of the Group 2 and Group 12 cations[a,b]

M^+	ns^0np^1	$(n\text{-}1)d^9ns^2$	ns^1nd^1
Group 2			
Be^+	31933		98055
Mg^+	35730		71491
Ca^+	25340		13687
Sr^+	24250		14724
Ba^+	21389		5354
Ra^+	24590		13079
Group 12			
Zn^+	49064	64354	96940
Cd^+	45791	72640	89782
Hg^+	57568	44539	105320

[a] Data taken from Ref. 65.

[b] Non-spin-orbit split energies, derived from the energies of the spin-orbit levels, assuming the latter are located at $E_0 = \frac{1}{2}\zeta[j(j+1) - l(l+1) - s(s+1)]$, where E_0 is the non-spin-orbit split energy, ζ is the spin-orbit coupling constant and *j*, *l* and *s* have their usual meanings.

Table 5: Partial atomic charges for the Group 2 M^+-RG complexes, calculated using NPA and AIM methodologies, in units of elementary charge *e*.

M	Method	Charge	M^+-He	M^+-Ne	M^+-Ar	M^+-Kr	M^+-Xe	M^+-Rn
Be	Q_{Be}	Mulliken	1.00	0.97	0.82	0.97	0.52	0.42
		NPA	1.00	0.99	0.91	0.88	0.82	0.79
		AIM	1.00	1.02	1.02	1.00	0.98	0.97
	Q_{RG}	Mulliken	0.00	0.03	0.18	0.03	0.48	0.58
		NPA	0.00	0.01	0.09	0.12	0.18	0.21
		AIM	0.00	-0.02	-0.02	0.00	0.02	0.03
Mg	Q_{Mg}	Mulliken	1.00	0.98	0.97	0.93	0.83	0.75
		NPA	1.00	1.00	0.98	0.97	0.93	0.92
		AIM	1.00	1.01	1.02	1.02	1.00	0.99
	Q_{RG}	Mulliken	0.00	0.02	0.03	0.07	0.17	0.25
		NPA	0.00	0.00	0.02	0.03	0.07	0.08
		AIM	0.00	-0.01	-0.02	-0.02	0.00	0.01
Ca	Q_{Ca}	Mulliken	1.00	0.99	0.96	0.95	0.92	0.88
		NPA	1.00	1.00	0.99	0.98	0.97	0.97
		AIM	1.00	1.01	1.02	1.02	1.01	1.00
	Q_{RG}	Mulliken	0.00	0.01	0.04	0.05	0.08	0.12
		NPA	0.00	0.00	0.01	0.02	0.03	0.03
		AIM	0.00	-0.01	-0.02	-0.02	-0.01	0.00
Sr	Q_{Sr}	Mulliken	1.00	0.99	0.98	0.99	0.94	0.85
		NPA	1.00	1.00	1.00	1.01	0.97	0.92
		AIM	1.00	1.01	1.03	1.04	1.00	0.96
	Q_{RG}	Mulliken	0.00	0.01	0.02	0.01	0.06	0.15
		NPA	0.00	0.00	0.00	-0.01	0.03	0.08
		AIM	0.00	-0.01	-0.03	-0.04	0.00	0.04
Ba	Q_{Ba}	Mulliken	1.00	0.99	0.98	0.98	0.97	0.93
		NPA	1.00	1.00	1.00	0.98	0.99	0.98
		AIM	1.00	1.01	1.01	1.01	1.02	1.00
	Q_{RG}	Mulliken	0.00	0.01	0.02	0.02	0.03	0.07
		NPA	0.00	0.00	0.00	0.02	0.01	0.02
		AIM	0.00	-0.01	-0.01	-0.01	-0.02	0.00
Ra	Q_{Ra}	Mulliken	1.00	0.94	0.97	0.96	0.96	0.93
		NPA	1.00	0.94	0.99	0.99	0.99	0.98
		AIM	1.00	0.96	1.02	1.02	1.01	1.01
	Q_{RG}	Mulliken	0.00	0.06	0.03	0.04	0.04	0.07
		NPA	0.00	0.06	0.01	0.01	0.01	0.02
		AIM	0.00	0.04	-0.02	-0.02	-0.01	-0.01

Table 6: Partial atomic charges for the Group 12 M^+-RG complexes, calculated using NPA and AIM methodologies, in units of elementary charge *e*.

M	Charge	Method	M^+-He	M^+-Ne	M^+-Ar	M^+-Kr	M^+-Xe	M^+-Rn
Zn	Q_{Zn}	Mulliken	1.00	0.98	0.94	0.90	0.81	0.74
		NPA	1.00	0.99	0.94	0.90	0.82	0.77
		AIM	1.00	1.01	0.95	0.91	0.83	0.78
	Q_{RG}	Mulliken	0.00	0.02	0.06	0.10	0.19	0.26
		NPA	0.00	0.01	0.06	0.10	0.18	0.23
		AIM	0.00	-0.01	0.05	0.09	0.17	0.22
Cd	Q_{Cd}	Mulliken	1.00	0.99	0.96	0.92	0.87	0.80
		NPA	1.00	1.00	0.97	0.93	0.87	0.83
		AIM	1.00	1.01	0.97	0.93	0.86	0.82
	Q_{RG}	Mulliken	0.00	0.01	0.04	0.08	0.13	0.20
		NPA	0.00	0.00	0.03	0.07	0.13	0.17
		AIM	0.00	-0.01	0.03	0.07	0.14	0.18
Hg	Q_{Hg}	Mulliken	1.00	0.99	0.94	0.89	0.74	0.64
		NPA	1.00	1.00	0.95	0.89	0.74	0.70
		AIM	1.00	1.00	0.95	0.87	0.74	0.66
	Q_{RG}	Mulliken	0.00	0.01	0.06	0.11	0.26	0.36
		NPA	0.00	0.00	0.05	0.11	0.26	0.30
		AIM	0.00	0.00	0.05	0.13	0.26	0.34

Table 7: Input Parameters for the electrostatic model potential (Eq. 2)[a]

Species	α_d/ Å^3	α_q/ Å^5	α_o/ Å^7	B (e^{-1} Å^6)	γ / e^{-2} Å^7	N	mass/ m_u
He	0.205	0.101	0.123	-0.144	0.501	1.434	4.00
Ne	0.396	0.27	0.397	-0.286	1.383	4.45	20.2
Ar	1.64	2.08	6.16	-3.07	13.6	5.90	39.95
Kr	2.48	3.97	16.35	-6.53	30.2	6.70	83.8
Xe	4.04	8.8	42.7	-15.57	80.0	7.79	131.3
Rn	5.1	20	110	-40	134	9	222
Be^+	3.7	2.20				0.77	9.012
Mg^+	5.5	6.22				0.98	24.31
Ca^+	11	54				1.05	40.08
Sr^+	13.1	68				1.1	87.82
Ba^+	18.4	200				1.16	137.3
Ra^+	15.5	105.7				1.2	226.03
Zn^+	2.8	4				6	65.39
Cd^+	3.5	4.5				6.5	112.41
Hg^+	2.7	4				7	201.97

[a] See text for sources of values and definitions of quantities.

Table 8: Effective charges on M^+ from the electrostatic model potential (Eq. 2),[a] in units of elementary charge *e*.

M^+	Method	M^+-He	M^+-Ne	M^+-Ar	M^+-Kr	M^+-Xe	M^+-Rn
Group 2							
Be^+	undamped	1.03	0.97	0.67	0.88	1.06	0.99
	damped	1.05	1.43	0.82	1.02	1.20	1.18
Mg^+	undamped	1.05	0.99	0.86	0.89	0.97	0.91
	damped	1.05	1.03	0.92	0.93	1.00	0.96
Ca^+	undamped	1.08	1.09	0.64	0.71	0.82	0.79
	damped	1.08	1.14	0.72	0.76	0.86	0.84
Sr^+	undamped	1.10	1.15	0.69	0.75	0.84	0.80
	damped	1.10	1.19	0.74	0.79	0.87	0.84
Ba^+	undamped	1.12	1.19	-[b]	0.42	0.67	0.65
	damped	1.12	1.25	-[b]	0.46	0.71	0.69
Ra^+	undamped	1.14	1.17	0.88	0.87	0.91	0.87
	damped	1.14	1.17	0.91	0.89	0.93	0.90
Group 12							
Zn^+	undamped	1.05	0.97	0.96	1.01	1.12	1.06
	damped	1.06	0.99	0.99	1.04	1.16	1.13
Cd^+	undamped	1.08	1.01	1.02	1.04	1.12	1.06
	damped	1.09	1.01	1.03	1.05	1.13	1.10
Hg^+	undamped	1.12	1.06	1.10	1.15	1.29	1.25
	damped	1.12	1.07	1.11	1.16	1.30	1.29

[a] See text.

[b] No solution – see text.

Table 9: Local energy densities $H(R)$ for the Group 2 and 12 M^+-RG complexes.[a]

	He	Ne	Ar	Kr	Xe	Rn
Group 2						
Be^+	0.0006	-0.0022	-0.0025	-0.0071	-0.0116	-0.0133
Mg^+	0.0002	0.0000	0.0001	-0.0001	-0.0009	-0.0014
Ca^+	0.0001	0.0002	0.0020	0.0017	0.0011	0.0007
Sr^+	0.0001	0.0002	0.0016	0.0014	0.00010	0.0007
Ba^+	0.0001	0.0002	0.0021	0.0014	0.0008	0.0006
Ra^+	0.0001	0.0001	0.0011	0.0011	0.0008	0.0006
Group 12						
Zn^+	0.0008	0.0006	-0.0029	-0.0064	-0.0084	-0.0089
Cd^+	0.0008	0.0007	0.0005	-0.0018	-0.0037	-0.0044
Hg^+	0.0013	0.0011	-0.0002	-0.0040	-0.0071	-0.0080

[a] Calculated at the bond critical points from the AIM analyses.

Figure Captions

Figure 1: Interaction energy curves for the Group 2 M^+-RG complexes.

Figure 2: Interaction energy curves for the Group 12 M^+-RG complexes.

Figure 3: Reduced potentials for the Group 2 M^+-RG complexes.

Figure 4: Reduced potentials for the Group 12 M^+-RG complexes.

Figure 5: Plots of κ (see Eq. 1) for Group 2 and Group 12 M^+-RG complexes.

Figure 6: Trends in R_e for the Group 2 and Group 12 M^+-RG complexes.

Figure 7: Trends in D_e for the Group 2 and Group 12 M^+-RG complexes.

Figure 8: Trends in k for the Group 2 and Group 12 M^+-RG complexes.

Figure 9: MO diagram and contour plots for the Be^+-RG and Mg^+-RG complexes calculated at the RCCSD(T) R_e values obtained at the extrapolated basis set limit. The values of the contours were selected both to show the details clearly for all complexes, and are identical to allow direct comparison between the plots. The different colours indicate opposite signs of the wavefunction.

Figure 10: MO diagram and contour plots for the Ca^+-RG and Zn^+-RG complexes calculated at the RCCSD(T) R_e values obtained at the extrapolated basis set limit. The values of the contours were selected both to show the details clearly for all complexes, and are identical to allow direct comparison between the plots. The different colours indicate opposite signs of the wavefunction.

Figure 11: MO diagram and contour plots for the Sr^+-RG and Cd^+-RG complexes calculated at the RCCSD(T) R_e values obtained at the extrapolated basis set limit. The values of the contours were selected both to show the details clearly for all complexes, and are identical to allow direct comparison between the plots. The different colours indicate opposite signs of the wavefunction.

Figure 12: MO diagram and contour plots for the Ba^+-RG and Hg^+-RG complexes calculated at the RCCSD(T) R_e values obtained at the extrapolated basis set limit. The values of the contours were selected both to show the details clearly for all complexes, and are identical to allow direct comparison between the plots. The different colours indicate opposite signs of the wavefunction.

Figure 13: Birge-Sponer Plots for Be^+-RG and Mg^+-RG. The red dots are the calculated spacings between consecutive vibrational levels, while the line is a Morse line calculated from the ω_e and $\omega_e x_e$ values given in Table 1 (see text).

Figure 14: Birge-Sponer Plots for Ca^+-RG and Zn^+-RG. The red dots are the calculated spacings between consecutive vibrational levels, while the line is a Morse line calculated from the ω_e and $\omega_e x_e$ values given in Tables 1 and 2 (see text).

Figure 15: Birge-Sponer Plots for Sr^+-RG and Cd^+-RG. The red dots are the calculated spacings between consecutive vibrational levels, while the line is a Morse line calculated from the ω_e and $\omega_e x_e$ values given in Tables 1 and 2 (see text).

Figure 16: Birge-Sponer Plots for Ba^+-RG and Hg^+-RG. The red dots are the calculated spacings between consecutive vibrational levels, while the line is a Morse line calculated from the ω_e and $\omega_e x_e$ values given in Tables 1 and 2 (see text).

Figure 1

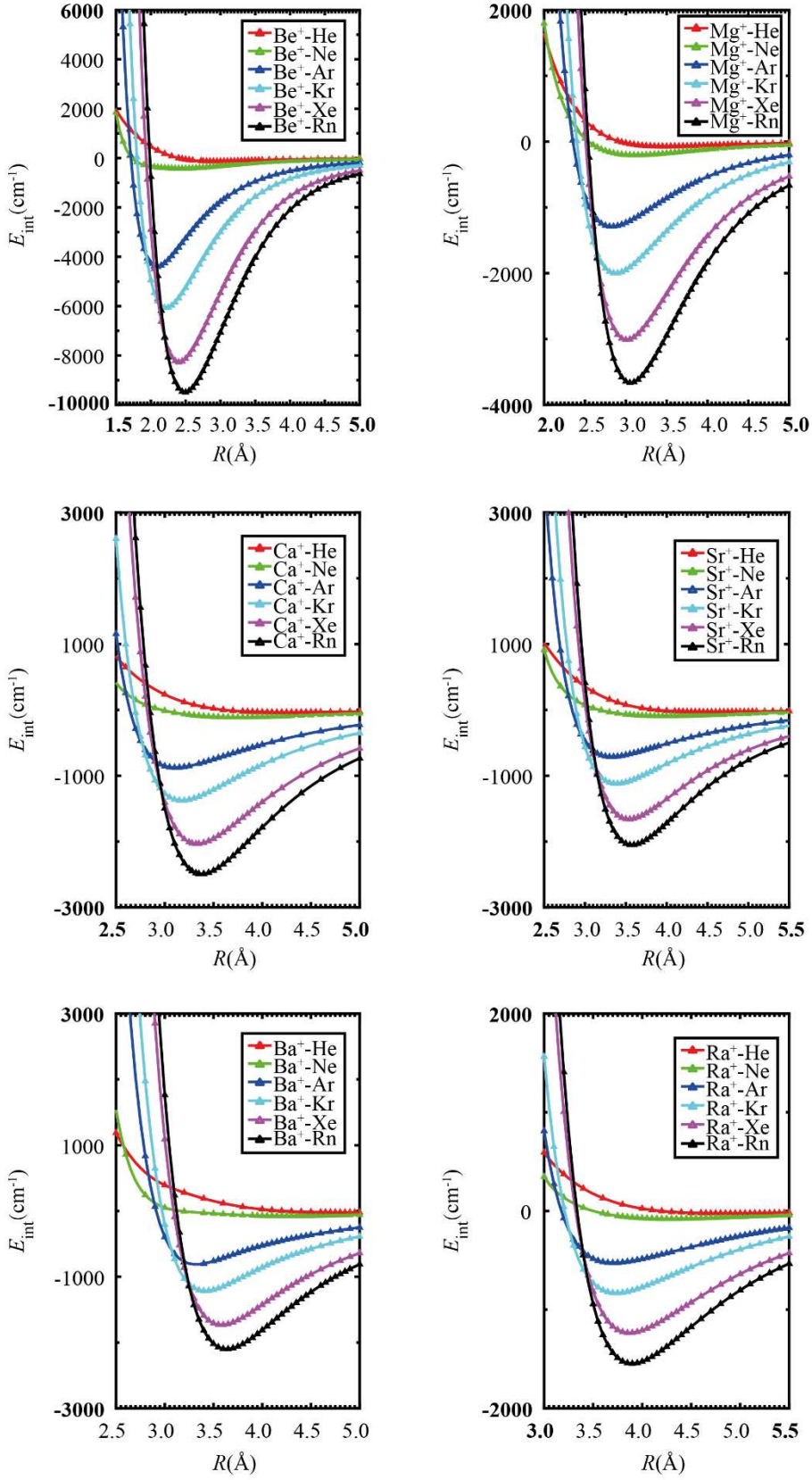
Be+-He
Be+-Ne
Be+-Ar
Be+-Kr
Be+-Xe
Be+-Rn
Mg+-He
Mg+-Ne
Mg+-Ar
Mg+-Kr
Mg+-Xe
Mg+-Rn
Ca+-He
Ca+-Ne
Ca+-Ar
Ca+-Kr
Ca+-Xe
Ca+-Rn
Sr+-He
Sr+-Ne
Sr+-Ar
Sr+-Kr
Sr+-Xe
Sr+-Rn
Ba+-He
Ba+-Ne
Ba+-Ar
Ba+-Kr
Ba+-Xe
Ba+-Rn
Ra+-He
Ra+-Ne
Ra+-Ar
Ra+-Kr
Ra+-Xe
Ra+-Rn
Eint(cm-1)
R(Å)

Figure 2

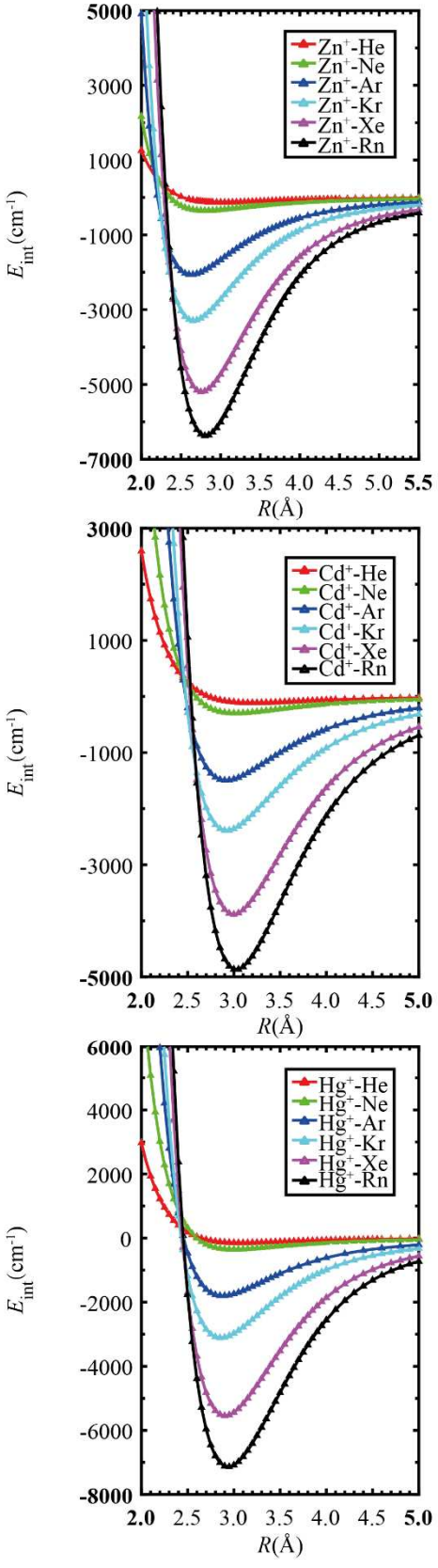
5000
3000
1000
-1000
-3000
-5000
-7000
2.0 2.5 3.0 3.5 4.0 4.5 5.0 5.5
R(Å)
E_int (cm^-1)
Zn+-He
Zn+-Ne
Zn+-Ar
Zn+-Kr
Zn+-Xe
Zn+-Rn
3000
1000
-1000
-3000
-5000
2.0 2.5 3.0 3.5 4.0 4.5 5.0
R(Å)
E_int (cm^-1)
Cd+-He
Cd+-Ne
Cd+-Ar
Cd+-Kr
Cd+-Xe
Cd+-Rn
6000
4000
2000
0
-2000
-4000
-6000
-8000
2.0 2.5 3.0 3.5 4.0 4.5 5.0
R(Å)
E_int (cm^-1)
Hg+-He
Hg+-Ne
Hg+-Ar
Hg+-Kr
Hg+-Xe
Hg+-Rn

Figure 3

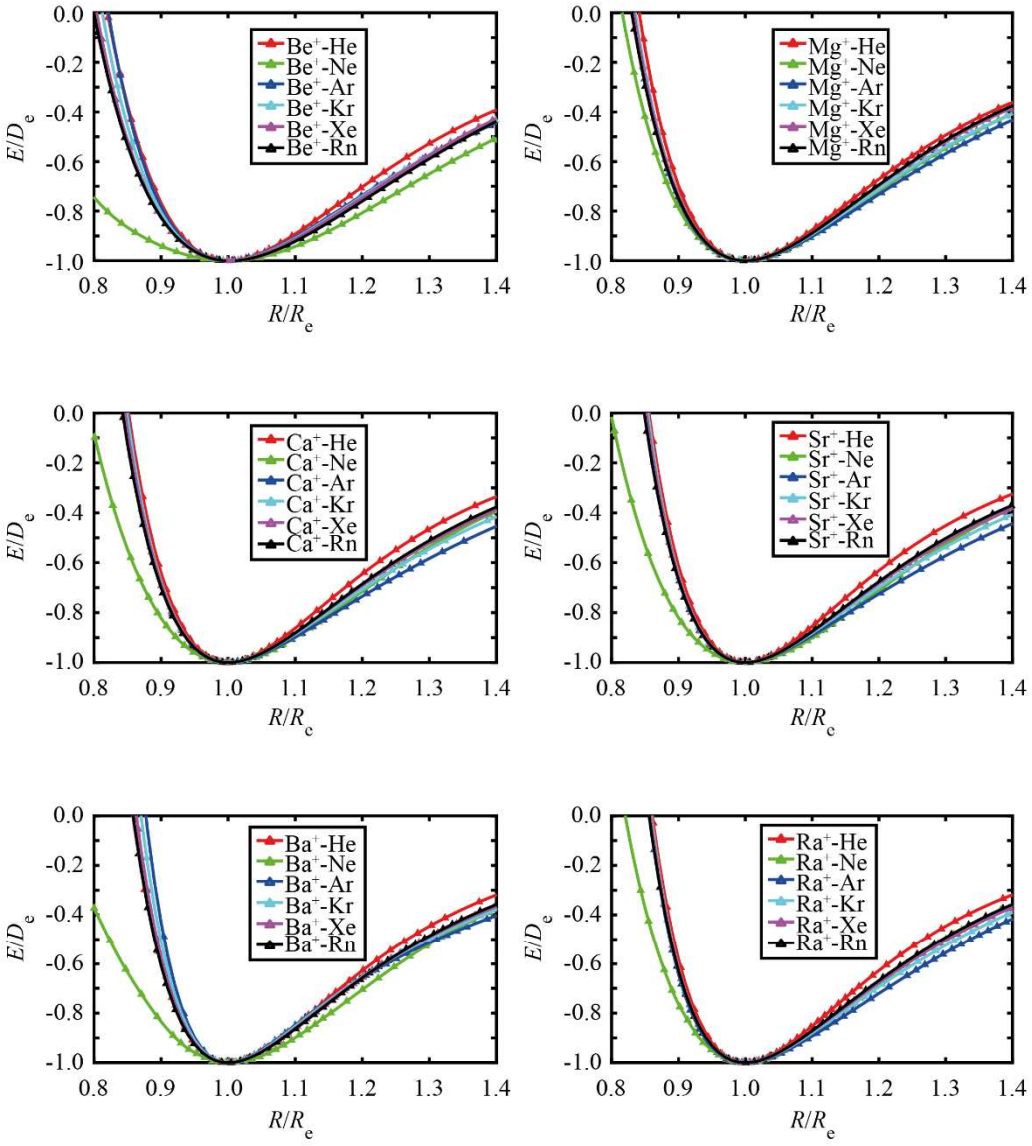
Be+-He
Be+-Ne
Be+-Ar
Be+-Kr
Be+-Xe
Be+-Rn
Mg+-He
Mg+-Ne
Mg+-Ar
Mg+-Kr
Mg+-Xe
Mg+-Rn
Ca+-He
Ca+-Ne
Ca+-Ar
Ca+-Kr
Ca+-Xe
Ca+-Rn
Sr+-He
Sr+-Ne
Sr+-Ar
Sr+-Kr
Sr+-Xe
Sr+-Rn
Ba+-He
Ba+-Ne
Ba+-Ar
Ba+-Kr
Ba+-Xe
Ba+-Rn
Ra+-He
Ra+-Ne
Ra+-Ar
Ra+-Kr
Ra+-Xe
Ra+-Rn
E/De
R/Re
0.0
-0.2
-0.4
-0.6
-0.8
-1.0
0.8
0.9
1.0
1.1
1.2
1.3
1.4

Figure 4

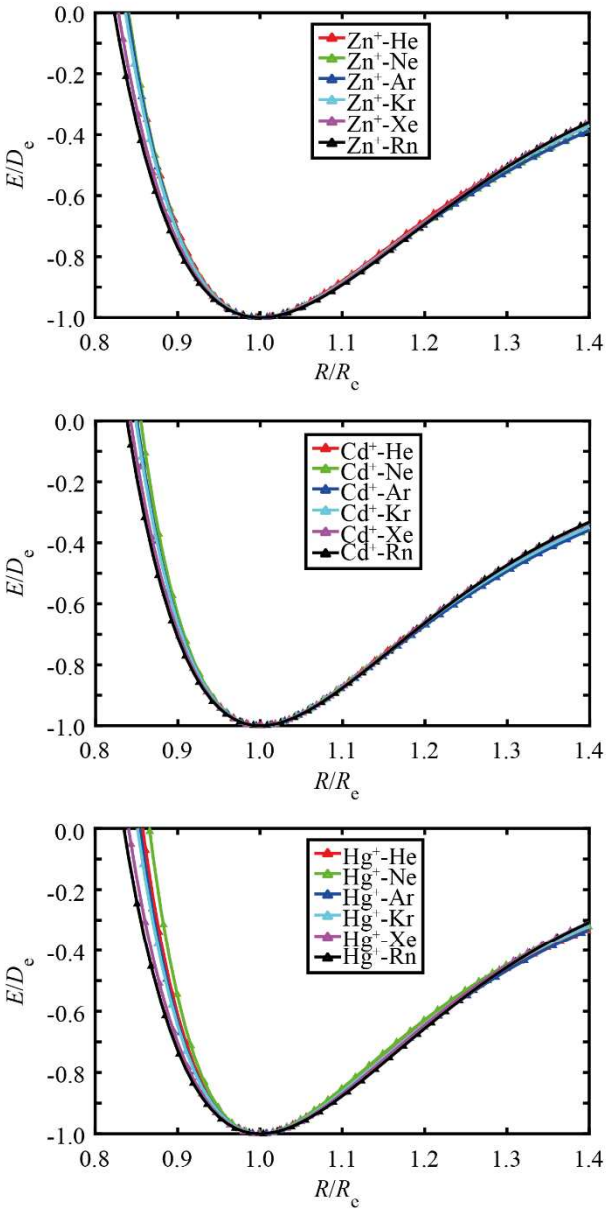
0.0
-0.2
-0.4
-0.6
-0.8
-1.0
E/D_e
0.8
0.9
1.0
1.1
1.2
1.3
1.4
R/R_e
Zn^+-He
Zn^+-Ne
Zn^+-Ar
Zn^+-Kr
Zn^+-Xe
Zn^+-Rn
Cd^+-He
Cd^+-Ne
Cd^+-Ar
Cd^+-Kr
Cd^+-Xe
Cd^+-Rn
Hg^+-He
Hg^+-Ne
Hg^+-Ar
Hg^+-Kr
Hg^+-Xe
Hg^+-Rn

Figure 5

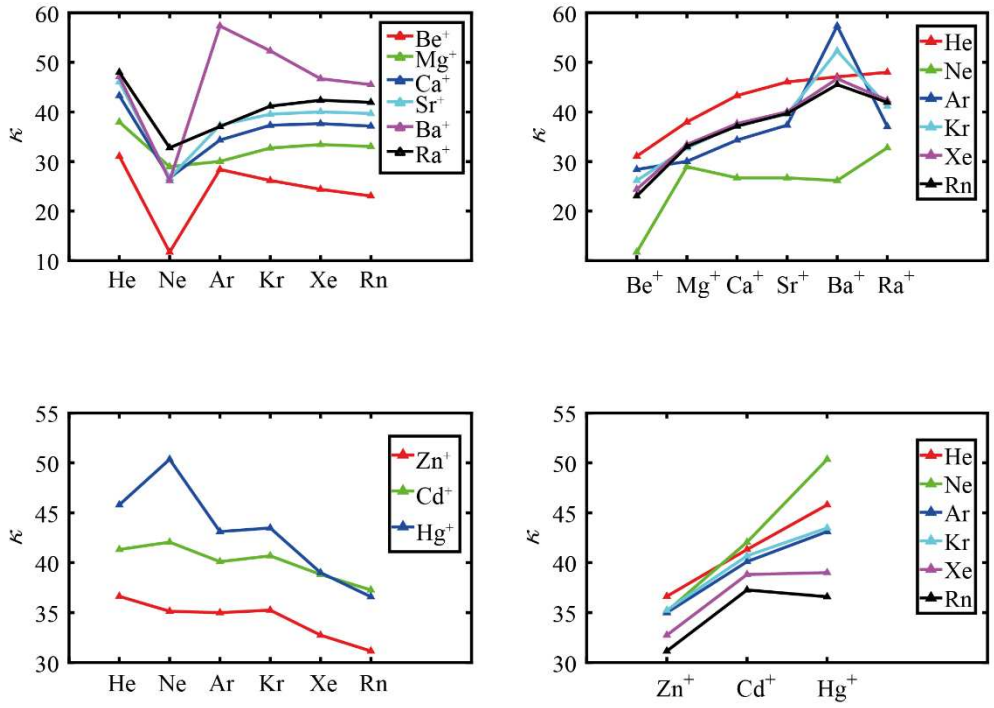
60
50
40
30
20
10
κ
Be+
Mg+
Ca+
Sr+
Ba+
Ra+
He Ne Ar Kr Xe Rn
He
Ne
Ar
Kr
Xe
Rn
Be+ Mg+ Ca+ Sr+ Ba+ Ra+
55
45
35
Zn+
Cd+
Hg+

Figure 6

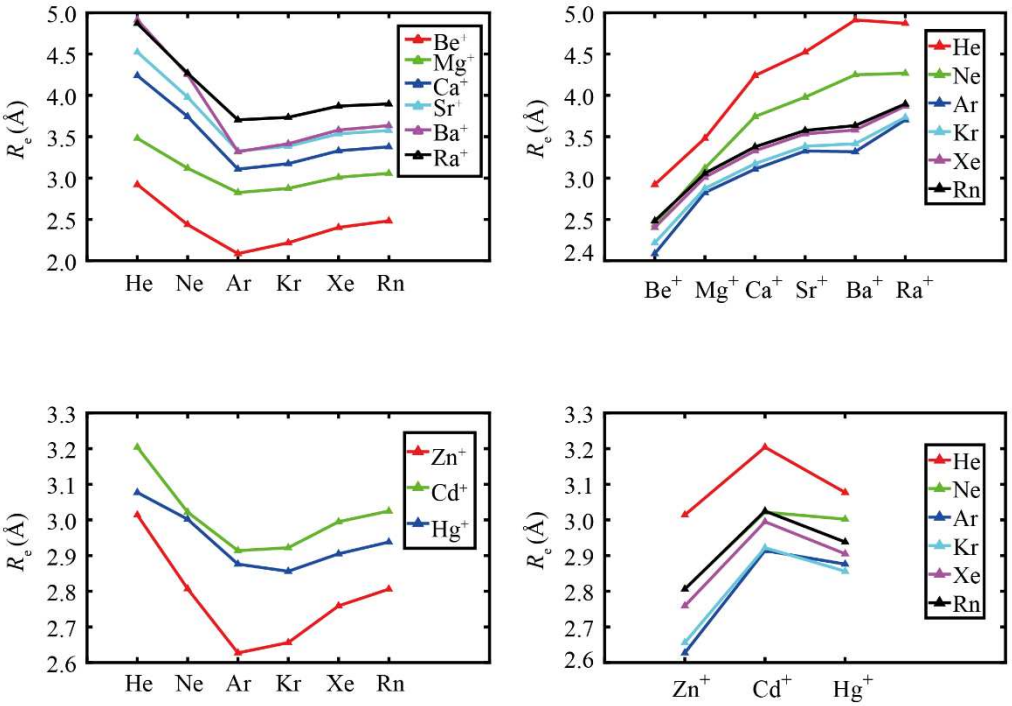
R_e (Å)
5.0
4.5
4.0
3.5
3.0
2.5
2.0
He Ne Ar Kr Xe Rn
Be^+
Mg^+
Ca^+
Sr^+
Ba^+
Ra^+
2.4
Be^+ Mg^+ Ca^+ Sr^+ Ba^+ Ra^+
He
Ne
Ar
Kr
Xe
Rn
3.3
3.2
3.1
3.0
2.9
2.8
2.7
2.6
Zn^+
Cd^+
Hg^+
Zn^+ Cd^+ Hg^+

Figure 7

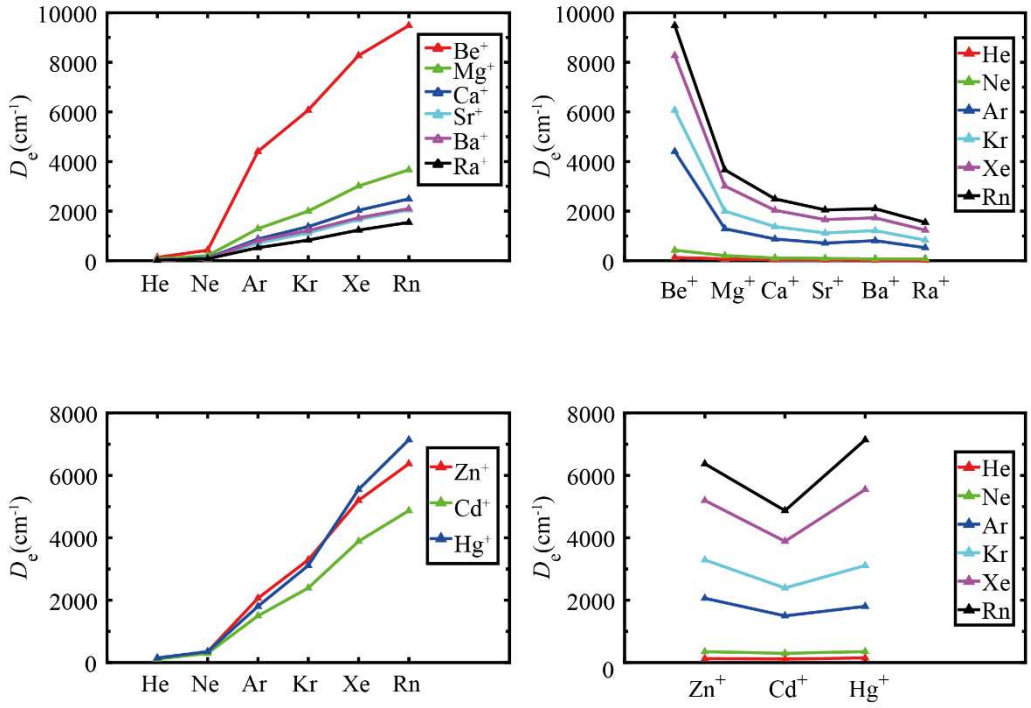
10000
8000
6000
4000
2000
0
D_e(cm^{-1})
Be$^+$
Mg$^+$
Ca$^+$
Sr$^+$
Ba$^+$
Ra$^+$
He Ne Ar Kr Xe Rn
He
Ne
Ar
Kr
Xe
Rn
Be$^+$ Mg$^+$ Ca$^+$ Sr$^+$ Ba$^+$ Ra$^+$
8000
6000
4000
2000
0
Zn$^+$
Cd$^+$
Hg$^+$
He Ne Ar Kr Xe Rn
Zn$^+$ Cd$^+$ Hg$^+$

Figure 8

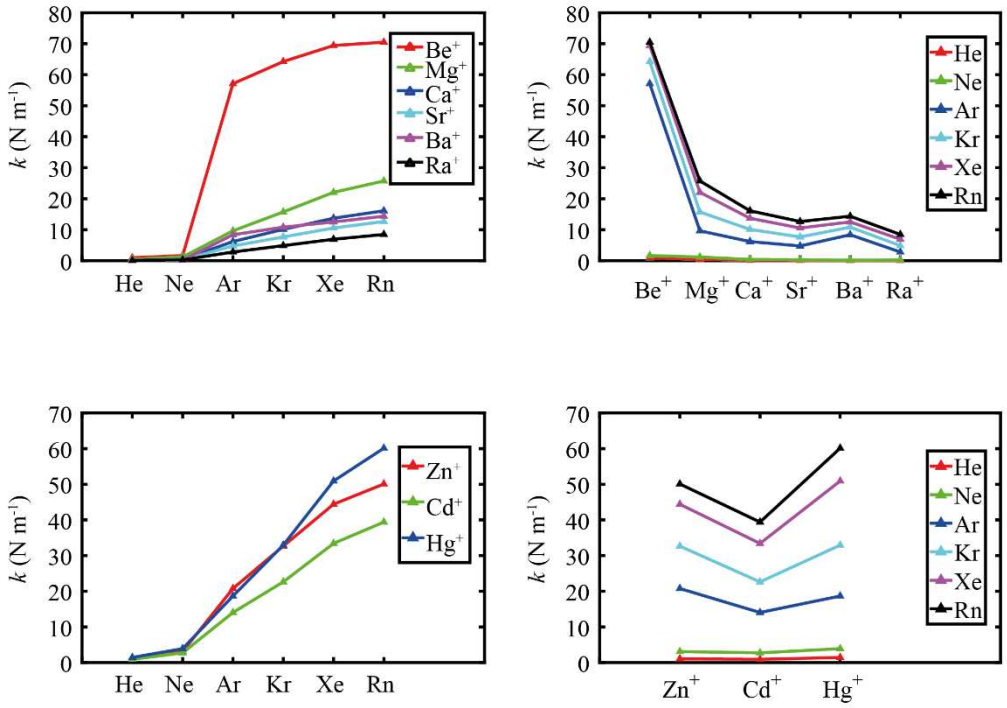

Figure 9

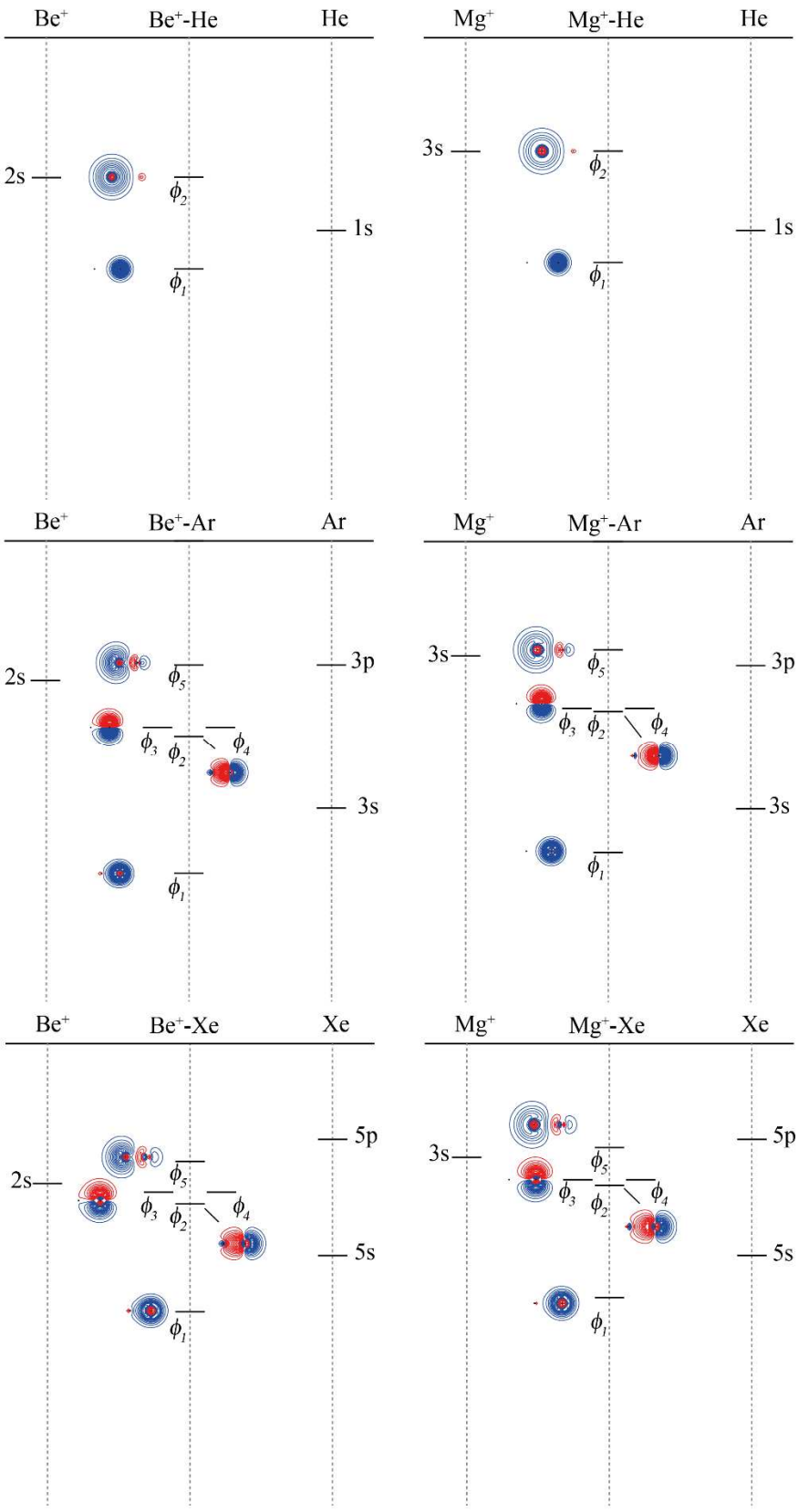
Be+
Be+-He
He
2s
1s
Mg+
Mg+-He
He
3s
1s
Be+
Be+-Ar
Ar
2s
3p
3s
Mg+
Mg+-Ar
Ar
3s
3p
3s
Be+
Be+-Xe
Xe
2s
5p
5s
Mg+
Mg+-Xe
Xe
3s
5p
5s

Figure 10

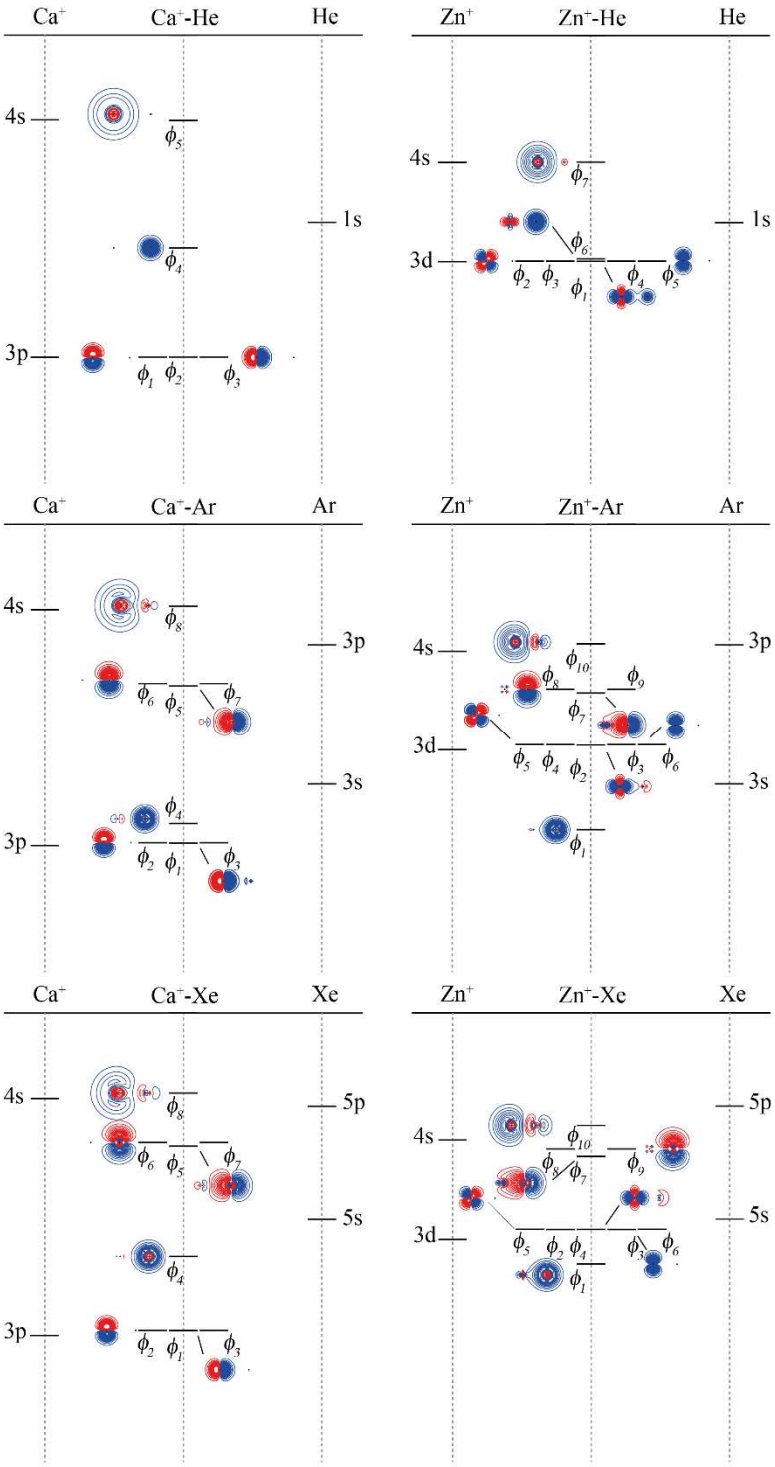
Ca+
Ca+-He
He
4s
1s
3p
Zn+
Zn+-He
He
4s
1s
3d
Ca+
Ca+-Ar
Ar
4s
3p
3s
3p
Zn+
Zn+-Ar
Ar
4s
3p
3d
3s
Ca+
Ca+-Xe
Xe
4s
5p
5s
3p
Zn+
Zn+-Xe
Xe
4s
5p
3d
5s

Figure 11

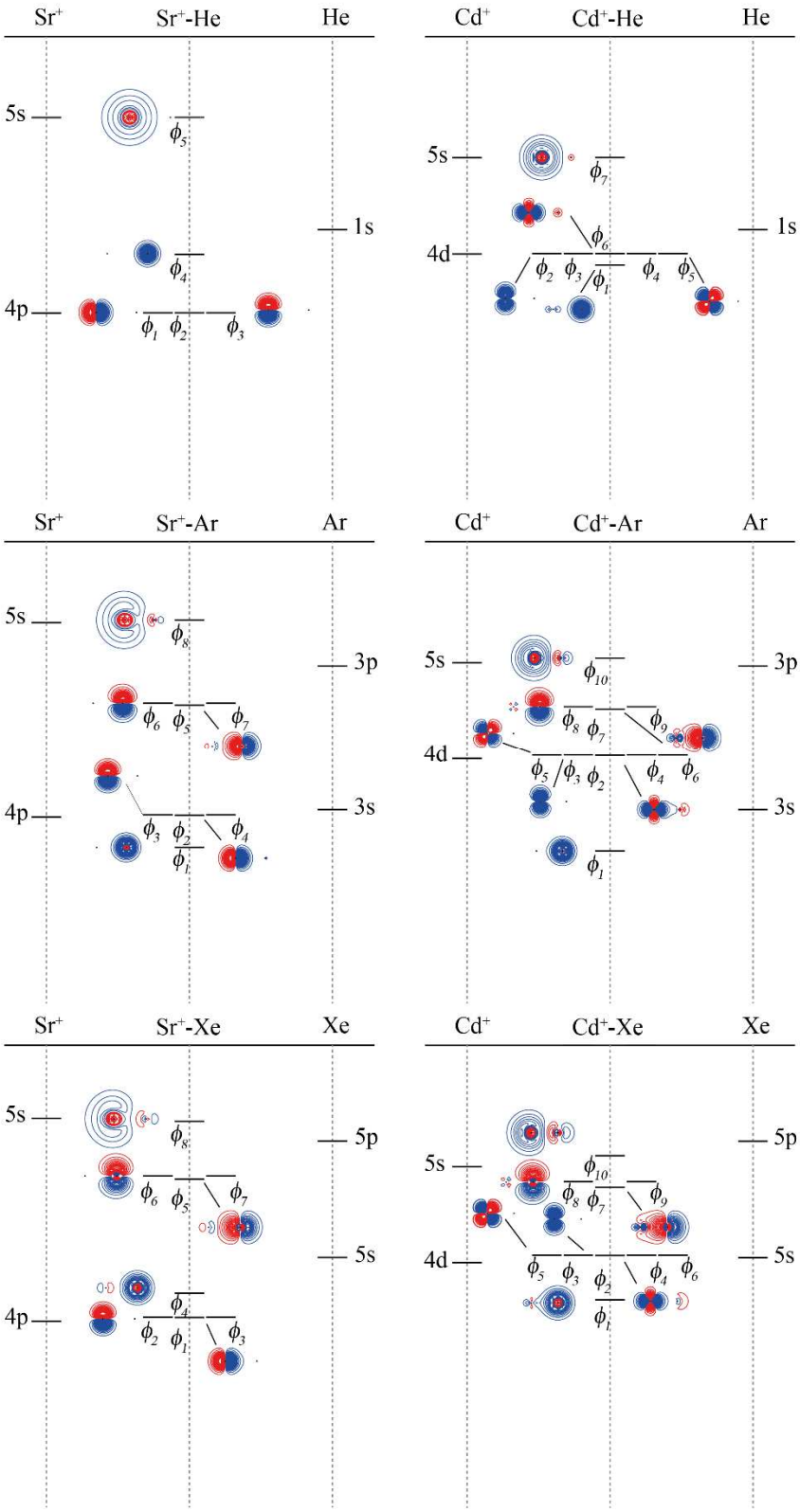
Sr+
Sr+-He
He
5s
4p
1s
Cd+
Cd+-He
He
5s
4d
1s
Sr+
Sr+-Ar
Ar
5s
4p
3p
3s
Cd+
Cd+-Ar
Ar
5s
4d
3p
3s
Sr+
Sr+-Xe
Xe
5s
4p
5p
5s
Cd+
Cd+-Xe
Xe
5s
4d
5p
5s

Figure 12

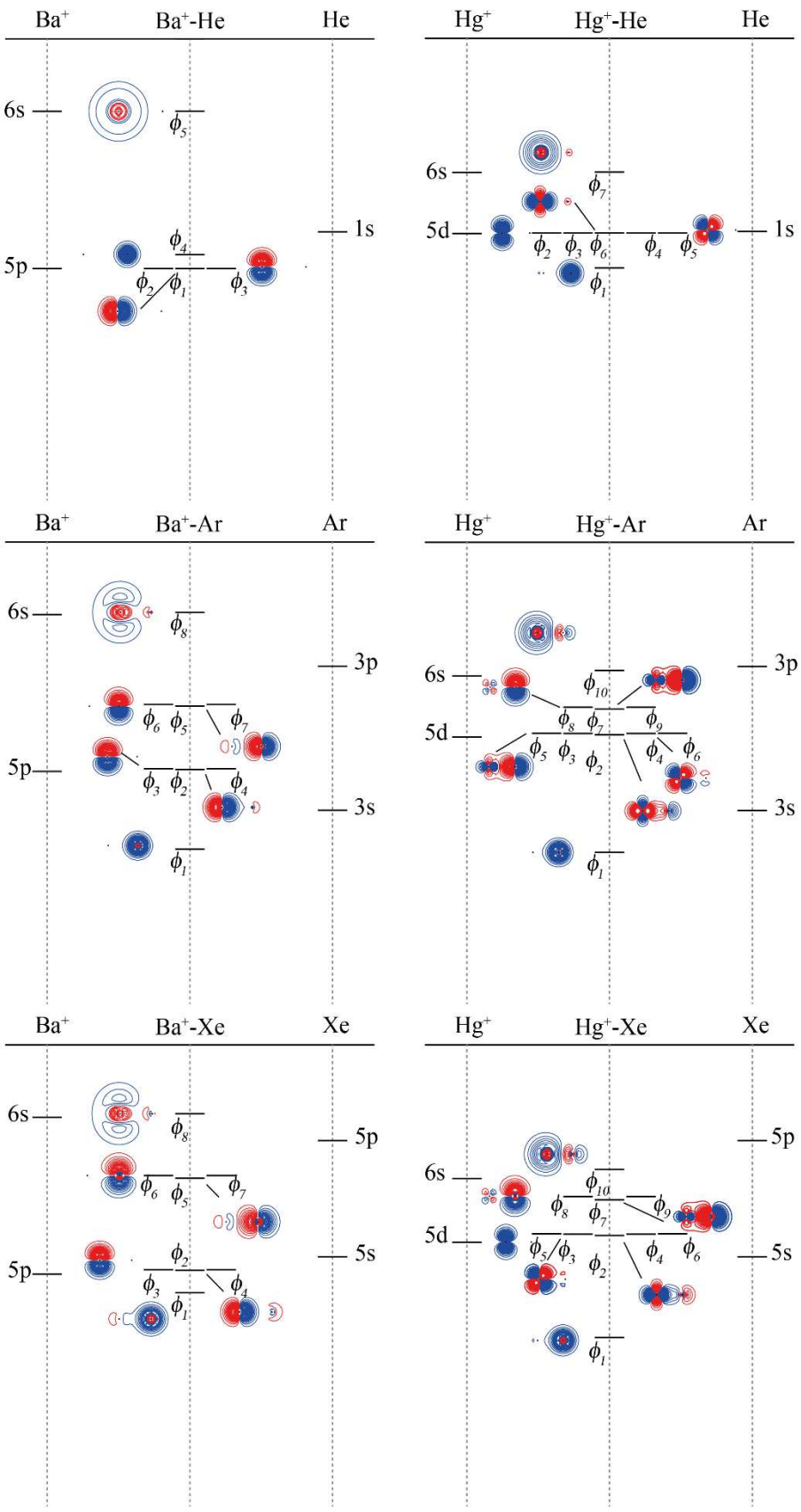
Ba+
Ba+-He
He
6s
5p
1s
Hg+
Hg+-He
He
6s
5d
1s
Ba+
Ba+-Ar
Ar
6s
5p
3p
3s
Hg+
Hg+-Ar
Ar
6s
5d
3p
3s
Ba+
Ba+-Xe
Xe
6s
5p
5p
5s
Hg+
Hg+-Xe
Xe
6s
5d
5p
5s

Figure 13

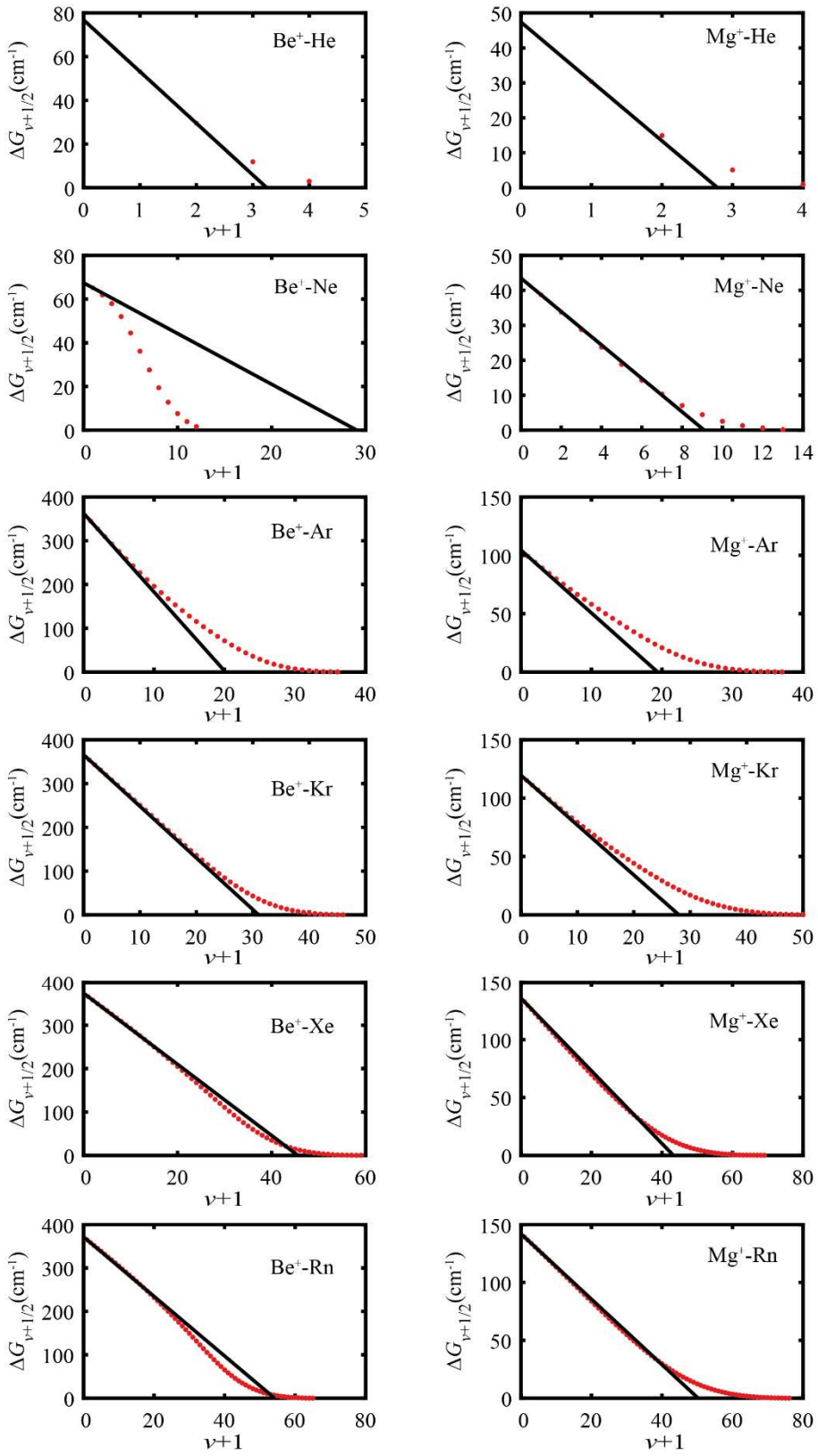
Be+-He
Mg+-He
Be+-Ne
Mg+-Ne
Be+-Ar
Mg+-Ar
Be+-Kr
Mg+-Kr
Be+-Xe
Mg+-Xe
Be+-Rn
Mg+-Rn
ΔGv+1/2(cm-1)
v+1

Figure 14

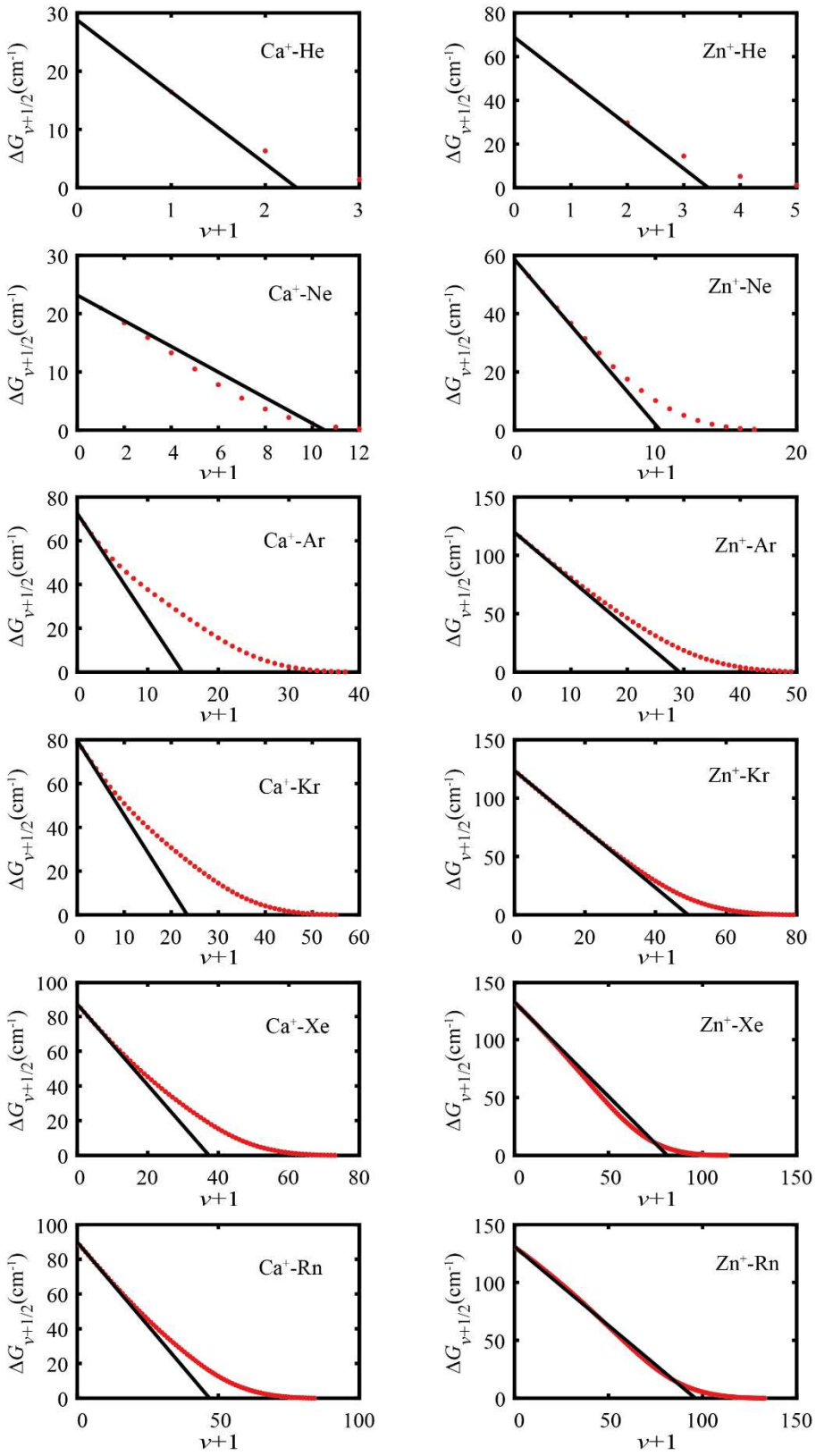
Ca+-He
Zn+-He
Ca+-Ne
Zn+-Ne
Ca+-Ar
Zn+-Ar
Ca+-Kr
Zn+-Kr
Ca+-Xe
Zn+-Xe
Ca+-Rn
Zn+-Rn
ΔGv+1/2(cm-1)
v+1

Figure 15

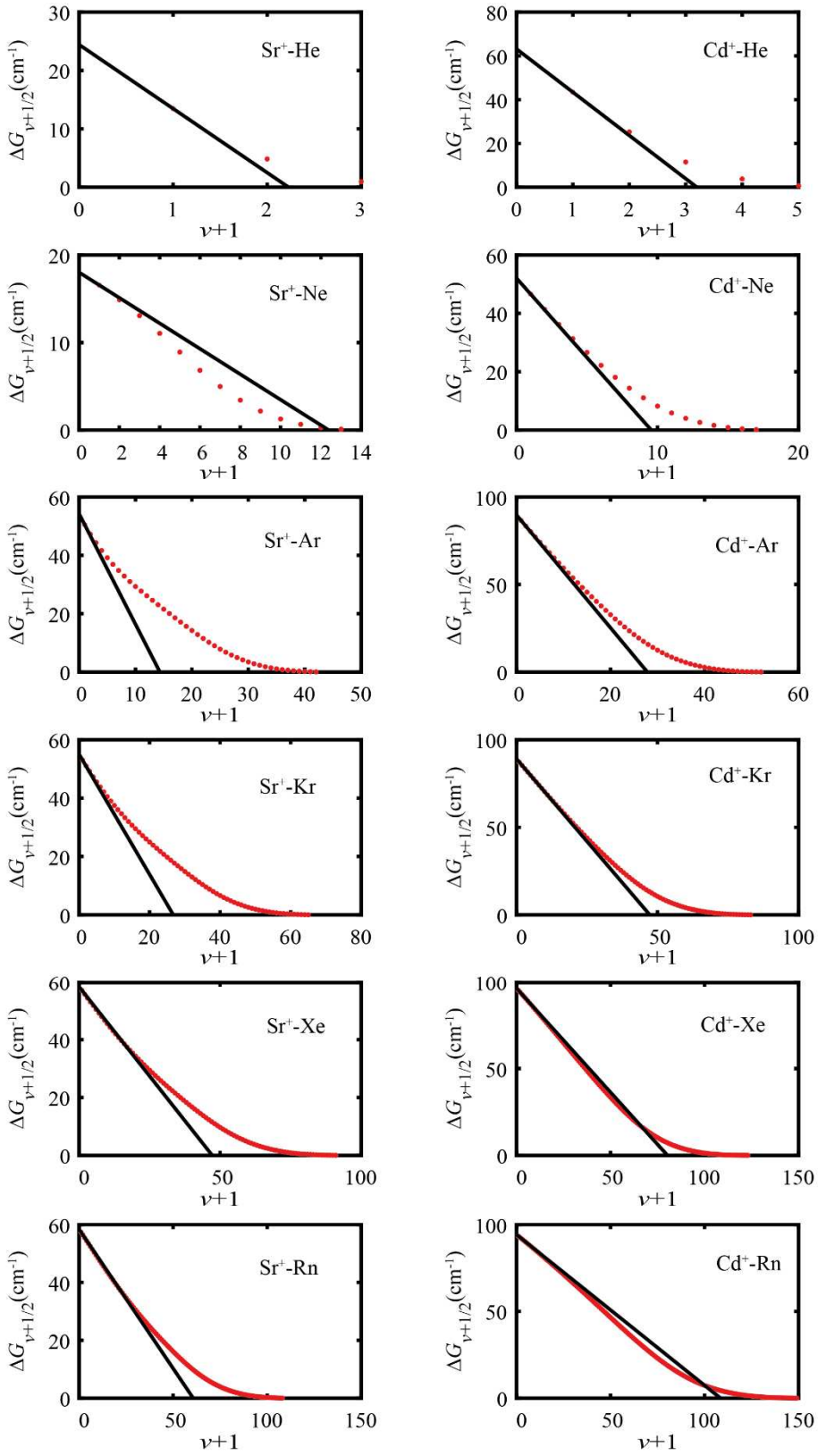
Sr+-He
Cd+-He
Sr+-Ne
Cd+-Ne
Sr+-Ar
Cd+-Ar
Sr+-Kr
Cd+-Kr
Sr+-Xe
Cd+-Xe
Sr+-Rn
Cd+-Rn
ΔGv+1/2(cm-1)
v+1

Figure 16

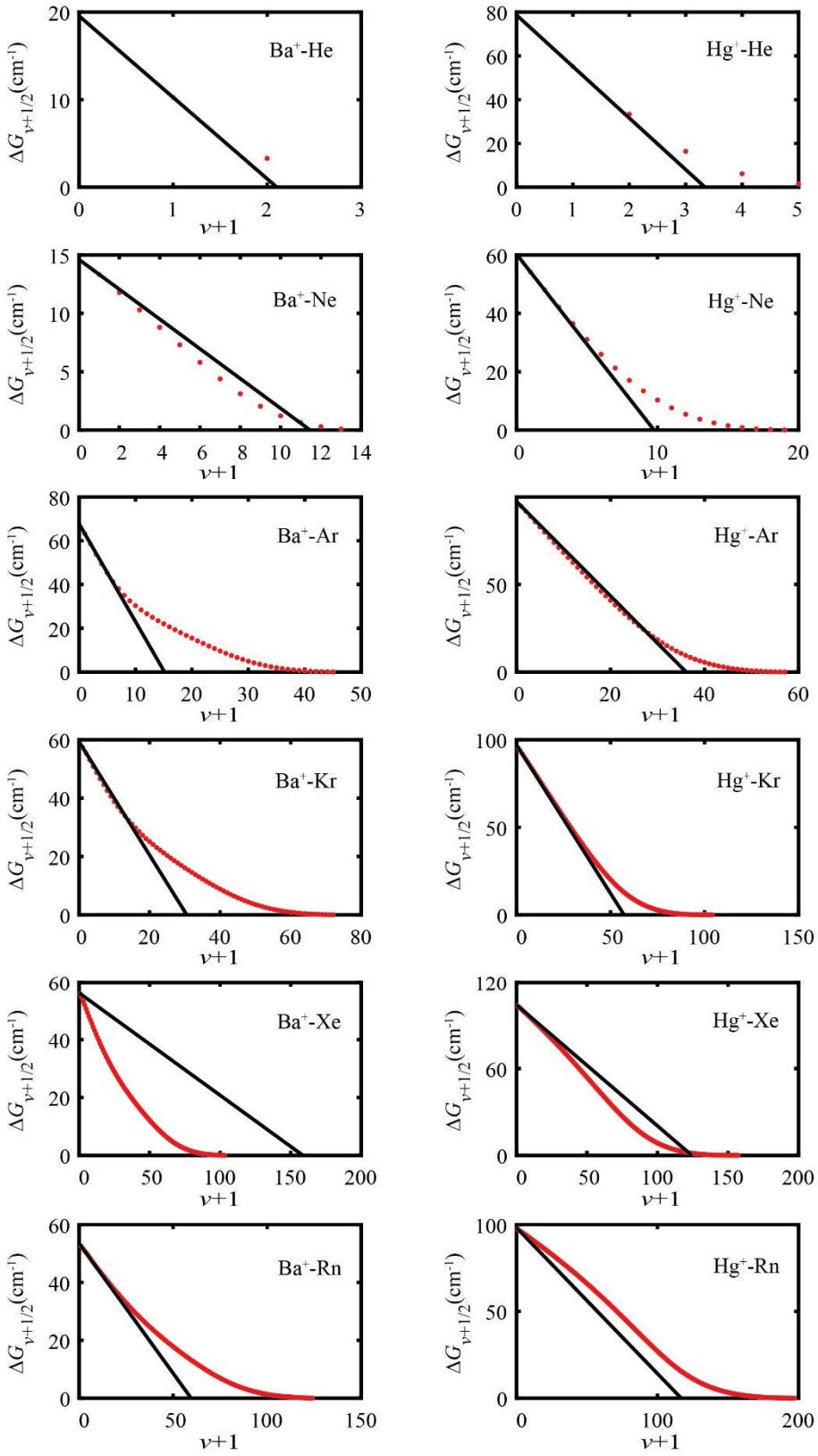
Ba+-He
Hg+-He
Ba+-Ne
Hg+-Ne
Ba+-Ar
Hg+-Ar
Ba+-Kr
Hg+-Kr
Ba+-Xe
Hg+-Xe
Ba+-Rn
Hg+-Rn
ΔGv+1/2(cm-1)
v+1

Table of Contents Graphic

References

[1] Soldán, P.; Lee, E. P. F.; Lozeille, J.; Murrell, J. N.; Wright, T. G. High-Quality potential for Li^+·He. *Chem. Phys. Lett.* **2001**, *343*, 429–436.

[2] Lozeille, J.; Winata, E.; Soldán, P.; Lee, E. P. F.; Viehland, L. A.; Wright, T. G. Spectroscopy of Li^+.Rg Complexes and Transport Properties of Li^+-Rg (Rg = He–Rn). *Phys. Chem. Chem. Phys.* **2002**, *4*, 3601–3610.

[3] Viehland, L. A.; Lozeille, J.; Soldán, P.; Lee, E. P. F.; Wright, T. G. Spectroscopy of Na^+.Rg and Transport Coefficients of Na^+ in Rg (Rg = He–Rn). *J. Chem. Phys.* **2003**, *119*, 3729–3736.

[4] Viehland, L. A.; Lozeille, J.; Soldán, P.; Lee; E. P. F.; Wright, T. G. Spectroscopy of K^+.Rg and Transport Coefficients of K^+ in Rg (Rg = He–Rn). *J. Chem. Phys.* **2004**, *121*, 341–351.

[5] Hickling, H. L.; Viehland, L. A.; Shepherd, D. T.; Soldán, P.; Lee, E. P. F.; Wright, T. G. Spectroscopy of M^+.Rg and Transport Coefficients of M^+ in Rg (M = Rb–Fr; Rg = He–Rn). *Phys. Chem. Chem. Phys.* **2004**, *6*, 4233–4239.

[6] Breckenridge, W. H.; Ayles, V. L.; Wright, T. G. Analysis of the Bonding in Alkali-Cation/Rg Complexes (Rg = He–Xe) Using a Simple Model Potential. *Chem. Phys.* **2007**, *333*, 77–84.

[7] McGuirk, M. F.; Viehland, L. A.; Lee, E. P. F.; Breckenridge, W. H.; Withers, C. D.; Gardner, A. M.; Plowright, R. J.; Wright, T. G. Theoretical Study of Ba^{n+}-RG Complexes and Transport of Ba^{n+} Through RG (n = 1,2; RG = He–Rn). *J. Chem. Phys*. **2009**, *130*, 194305.

[8] Gardner, A. M.; Withers, C. D.; Wright, T. G.; Kaplan, K. I.; Chapman, C. Y. N.; Viehland, L. A.; Lee, E. P. F.; Breckenridge, W. H. Theoretical Study of the Bonding in M^{n+}-RG Complexes and the Transport of M^{n+} Through RG (M = Ca, Sr, Ra; n = 1,2; RG = He–Rn). *J. Chem. Phys.* **2010**, *132*, 054302.

[9] Gardner, A. M.; Withers, C. D.; Graneek, J. B.; Wright, T. G.; Viehland, L. A.; Breckenridge, W. H. Theoretical Study of M^+-RG and M^{2+}-RG Complexes and Transport of M^+ through RG (M = Be and Mg; RG = He–Rn). *J. Phys. Chem. A* **2010**, *114*, 7631–7641.

[10] Yousef, A.; Shrestha, S.; Viehland, L. A.; Lee, E. P. F.; Gray, B. R.; Ayles, V. L.; Wright, T. G.; Breckenridge, W. H. Interaction Potentials and Transport Properties of Coinage Metal Cations in Rare Gases. *J. Chem. Phys.* **2007**, *127*, 154309.

[11] Breckenridge, W. H.; Ayles; V. L.; Wright, T. G. Evidence for Emergent Chemical Bonding in Au^+-Rg Complexes. *J. Phys. Chem. A* **2008**, *112*, 4209–4214.

[12] Qing, E.; Viehland, L. A.; Lee, E. P. F.; Wright, T. G. Interaction Potentials and Spectroscopy of Hg^+.Rg and Cd^+.Rg; and Transport Coefficients for Hg^+ and Cd^+ in Rg (Rg = He–Rn). *J. Chem. Phys.* **2006**, *124*, 044316.

[13] Lee, E. P. F.; Gray, B. R.; Joyner, N. A.; Johnson, S. H.; Viehland, L. A.; Breckenridge, W. H.; Wright, T. G. Accurate Potential Energy Curves for Zn^+-Rg (Rg = He–Rn): Spectroscopy and Transport Coefficients. *Chem. Phys. Lett.* **2007**, *450*, 19–24.

[14] Gray, B. R.; Lee, E. P. F.; Yousef, A.; Shrestha, S.; Viehland, L. A.; Wright, T. G. Accurate Potential Energy Curves for Tl^+-Rg (Rg = He–Rn): Spectroscopy and Transport Coefficients. *Mol. Phys.* **2006**, *104*, 3237–3244.

[15] Gardner, A. M.; Gutsmiedl, K. A.; Wright, T. G.; Breckenridge, W. H.; Chapman, C. Y. N.; Viehland, L. A. Theoretical Study of Al^+-RG (RG = He–Rn). *J. Chem. Phys.* **2010**, *133*, 164302.

[16] Gardner, A. M.; Gutsmiedl, K. A.; Wright, T. G.; Lee, E. P. F.; Breckenridge, W. H.; Rajbhandari, S.; Chapman, C. Y. N.; Viehland, L. A. Theoretical Study of M^+-RG Complexes (M = Ga, In; RG = He–Rn). *J. Phys. Chem. A* **2011**, *115*, 6979–6985.

[17] Harris, J. P.; Gardner, A. M.; Wright, T. G.; Breckenridge, W. H.; Viehland, L. A. Interactions in the B^+-RG Complexes and Comparison with Be^+-RG (RG = He–Rn): Evidence for Chemical Bonding. *J. Phys. Chem. A* **2012**, *116*, 4995–5007.

[18] Bellert, D.; Breckenridge, W. H. Bonding in Ground-State and Excited-State A^+·Rg van der Waals Ions (A = Atom, Rg = Rare-Gas Atom): A Model-Potential Analysis. *Chem. Rev.* **2002**, *102*, 1595–1622.

[19] Pyykkö, P. Predicted Chemical Bonds between Rare Gases and Au^+. *J. Am. Chem. Soc.*, **1995**, *117*, 2067–2070.

[20] Prascher, B. P.; Woon, D. E.; Peterson, K. A.; Dunning, Jr., T. H.; Wilson, A. K. Gaussian Basis Sets for Use in Correlated Molecular Calculations. VII. Valence, Core-Valence, and Scalar Relativistic Basis Sets for Li, Be, Na, and Mg *Theo. Chem. Acc.* **2011**, *128*, 69–82.

[21] Hill, J. G.; Peterson, K. A. Gaussian Basis Sets for Use in Correlated Molecular Calculations. XI. Pseudopotential-Based and All-Electron Relativistic Basis Sets for Alkali Metal (K–Fr) and Alkaline Earth (Ca–Ra) Elements. *J. Chem. Phys.* **2017**, *147*, 244106.

[22] Peterson, K. A.; Puzzarini, C. Systematically Convergent Basis Sets for Transition Metals. II. Pseudopotential-Based Correlation Consistent Basis Sets for the Group 11 (Cu, Ag, Au) and 12 (Zn, Cd, Hg) Elements. *Theor. Chem. Acc.* **2005**, *114*, 283–296.

[23] Halkier, A.; Helgaker, T.; Jørgensen, P.; Klopper, W.; Koch, H.; Olsen, J.; Wilson, A. K. Basis-Set Convergence in Correlated Calculations on Ne, N_2, and H_2O *Chem. Phys. Lett.* **1998**, *286*, 243–252.

[24] MOLPRO is a package of *ab initio* programs written by Werner, H.-J.; Knowles, P. J. et al.

[25] R. J. LeRoy, Level 8.0: A Computer Program for Solving the Radial Schrödinger Equation for Bound and Quasibound Levels, University of Waterloo Chemical Physics Research Report No. CP-663, 2007; see http://leroy.uwaterloo.ca/programs/.

[26] Schaftenaar, G.; Noordik, J. H. Molden: a Pre- and Post-Processing Program for Molecular and Electronic Structures. *J. Comput. Aided Mol. Des.* **2000**, *14*, 123–134.

[27] Mulliken, R. S. Electronic Population Analysis on LCAO–MO Molecular Wave Functions. I. J. Chem. Phys. **1955**, *23*, 1833–1840.

[28] Reed, A. E.; Weinstock, R. B.; Weinhold, F. Natural Population Analysis. J. Chem. Phys. **1985**, *83*, 735–746.

[29] Bader,R. F. W. *Atoms in Molecules — A Quantum Theory*; Oxford University Press: Oxford, U.K., 1990.

[30] Gaussian 09, Revision D.01, Frisch, M. J.; Trucks, G. W.; Schlegel, H. B.; Scuseria, G. E.; Robb, M. A. et al. Gaussian, Inc., Wallingford CT, 2009.

[31] Glendening, E. D.; Badenhoop, J. K.; Reed, A. E.; Carpenter, J. E.; Bohmann, J. A.; Morales, C. M.; Landis, C. R.; Weinhold, F. NBO 6.0, Theoretical Chemistry Institute, University of Wisconsin, Madison, 2013.

[32] Keith, T. A., AIMAll, T. K. Gristmill Software, Overland Park, KS, 2011, see aim.tkgristmill.com.

[33] Subbaram, K. V.; Coxon, J. A.; Jones W. E., Investigations of Metal Ion – Rare Gas Pairs by Optical Spectroscopy: High Resolution Analysis of the $A^2\Pi_r$–$X^2\Sigma^+$ System of $BeAr^+$. *Can J. Phys.* **1976**, *54*, 1535–1544.

[34] Coxon, J. A.; Jones, W. E.; Subbaram, K. V. Electronic Spectra of Metal Ion-Rare Gas Pairs: High Resolution Analysis of the $A^2\Pi_r$–$X^2\Sigma^+$ System of $BeKr^+$. *Can. J. Phys.* **1977**, *55*, 254–260.

[35] Coxon, J. A.; Jones, W. E.; Subbaram, K. V. First Observation of the $BeXe^+$ Molecule: The $A^2\Pi$–$X^2\Sigma$ Band System in Emission. *Can. J. Phys.* **1975**, *53*, 2321–2325.

[36] Reddic, J. E.; Duncan, M. A. Photodissociation Spectroscopy of the Mg^+-Ne Complex. *J. Chem. Phys.* **1999**, *110*, 9948–9955.

[37] Scurlock, C. T.; Pilgrim, J. S.; Duncan, M. A. Rotationally Resolved Photodissociation Spectroscopy of Mg^+-Ar. *J. Chem. Phys.* **1995**, *103*, 3293–3298. Erratum *J. Chem. Phys.* **1996**, *105*, 7876–7876.

[38] Pilgrim, J. S.; Yeh, C. S.; Berry, K. R.; Duncan, M. A. Photodissociation of Mg^+ Rare Gas Complexes. *J. Chem.Phys.* **1994**, *100*, 7945–7956.

[39] Kaup, J. G.; Breckenridge, W. H. Spectroscopic Characterization of the Metastable 3pπ $^3\Pi_{0^+,0^-}$ Valence States and the 4s $^3\Sigma^+$ Rydberg States of the MgKr and MgXe van der Waals Molecules *J. Chem. Phys.* **1997**, *107*, 10492–10505.

[40] Massick, S.; Breckenridge, W. H. A New Class of Strongly Bound, Doubly Excited Valence States of Neutral van der Waals Molecules: Mg(3pπ, 3pπ ^3P_J)–Ar($^3\Sigma^-$). *J. Chem. Phys.* **1996**, *104*, 7784-7787.

[41] Kaup, J. G.; Leung, A. W. K.; Breckenridge, W. H. Bond Energies of $MgKr^+$ and $MgXe^+$ from Resonant Two-Color Photoionization Thresholds. *J. Chem. Phys.* **1997**, *107*, 2180–2186.

[42] Reddic, J. E.; Pullins, S. H.; Duncan, M. A. Photodissociation Spectroscopy of the Ca^+-Ne Complex. *J. Chem. Phys.* **2000**, *112*, 4974–4982.

[43] Pullins, S. H.; Scurlock, C. T.; Reddic, J. E.; Duncan, M. A. Photodissociation Spectroscopy of Ca^+-Rare Gas Complexes. *J. Chem. Phys.* **1996**, *104*, 7518–7525.

[44] Kaup J. G.; Breckenridge, W. H. Bond Energies of $CaAr^+$, $CaKr^+$, and $CaXe^+$ from Resonant Two-Color Photoionization Thresholds. *J. Chem. Phys.* **1997**, *107*, 4451–4457.

[45] Kaup, J. G.; Breckenridge, W. H. Spectroscopic Characterization of the Metastable 4pπ $^2\Pi_0$-Valence States and the 5s $^3\Sigma^+$ Rydberg States of the CaAr, CaKr, and CaXe van der Waals Molecules. *J. Chem. Phys.*, **1997**, *107*, 5283–5289.

[46] Kaup, J. G.; Breckenridge, W. H. Spectroscopic Characterization of the Singly Excited CaAr(4dπ $^3\Pi_0$), CaAr(4dδ $^3\Delta_1$) States and the Doubly Excited CaAr(4pπ $^3\Sigma^-$) State. *J. Chem. Phys*. **1997**, *107*, 5676–5683.

[47] Lüder, C.; Prekas, D.; Vourliotaki, A.; Velegrakis, M. Photodissociation Spectrum of Sr^+Ne. *Chem. Phys. Lett.* **1997**, *267*, 149–154.

[48] Lüder, C.; Velegrakis, M. Photofragmentation Spectrum of the Sr^+Ar Complex. *J. Chem. Phys.* **1996**, *105*, 2167–2176.

[49] Prekas, D.; Feng, B.-H.; Velegrakis, M. Vibrational Constants and Binding Energies for the $A^2\Pi$ and $X^2\Sigma$ states of Sr^+Kr from Photodissociation Spectroscopy. *J. Chem. Phys.* **1998**, *108*, 2712–2717.

[50] Massaouti, M.; Sfounis, A.; Velegrakis, M. Vibrational Constants and Binding Energies of Sr^+Xe. *Chem. Phys. Lett.* **2001**, *348*, 47–52.

[51] Panov, S. I.; Williamson, J. M.; Miller, T. A. The Electronic Spectroscopy of the Ba^+-Ar Complex – Potential Energy Surface and Dissociation Energies. *J. Chem. Phys.* **1995**, *102*, 7359–7368.

[52] Viehland, L. A.; Hampt, D. S. The Distribution of Velocities for Ba^+ Ions in Ar Gas. *J. Chem. Phys.* **1992**, *97*, 4962–4973.

[53] Niu, X. H.; Shan, W. W.; Wang, S.; Shi, D. H. Accurate Spectroscopic Calculations on the $X^2\Sigma^+$, $A^2\Pi$, and $2^2\Sigma^+$ Electronic States of the $BeAr^+$ Cation Including Spin-Orbit Coupling. *Can. J. Chem.* **2014**, *92*, 397–405.

[54] Niu, X.; Zhu, Z.; Chen, Q. Ab Initio Study of the Low-Lying Electronic States of $[Be\text{-}Kr]^+$. *Chem. Phys. Lett.* **2015**, *619*, 208–213.

[55] Abdessalem, K.; Mejrissi, L.; Issaoui, N.; Oujia, B.; Gadéa, F. X. One and Two-Electron Investigation of Electronic Structure for Ba^+Xe and BaXe van der Waals Molecules in a Pseudopotential Approach. *J. Phys. Chem. A* **2013**, *117*, 8925–8938.

[56] Buchachenko, A. A.; Viehland, L. A. Interaction Potentials and Transport Properties of Ba, Ba^+, and Ba^{2+} in Rare Gases from He to Xe. *J. Chem. Phys.* **2018**, *148*, 154304.

[57] Goble, J. H.; Hartman, D. C.; Winn, J. S. Chemiluminescent Associative Ionization Reactions. *J. Chem. Phys*. **1977**, *66*, 363–364.

[58] Winn, J. S. A Systematic Look at Weakly Bound Diatomics. *Acc. Chem. Res.* **1981**, *14*, 341–348.

[59] Tellinghuisen, J.; Henderson, S. D.; Austin, D.; Lawley, K. P.; Donovan, R. J. Reduced Potential-Energy Curves for Diatomic-Molecules. *Phys. Rev. A* **1989**, *39*, 925–930.

[60] Van Hooydonk, G. A. Universal Two-Parameter Kratzer-Potential and Its Superiority over Morse's for Calculating and Scaling First-Order Spectroscopic Constants of 300 Diatomic Bonds. *Eur. J. Inorg. Chem*. **1999**, 1617–1642.

[61] Xie, R.-H.; Gong, J. Simple Three-Parameter Model Potential for Diatomic Systems: From Weakly and Strongly Bound Molecules to Metastable Molecular Ions. *Phys. Rev. Lett.* **2005**, *95*, 263202.

[62] Xie, R.-H.; Han, P. S. Universal Reduced Potential Function for Diatomic Systems *Phys. Rev. Lett.* **2006**, *96*, 243201.

[63] Sutherland, G. B. B. M. The Relation between the Force Constant, the Inter-Nuclear Distance, and the Dissociation Energy of a Diatomic Linkage. *Proc. Ind. Acad. Sci. A* **1938**, *8*, 341–344.

[64] Wright; T. G.; Breckenridge, W. H. The Radii of Atomic Ions Determined From Diatomic Ion-He Bond Lengths. *J. Phys. Chem. A* **2010**, *114*, 3182–3189.

[65] Kramida, A.; Ralchenko, Yu.; Reader, J. and NIST ASD Team (2018). NIST Atomic Spectra Database (ver. 5.5.6), [Online]. Available: https://physics.nist.gov/asd [2018, July 6]. National Institute of Standards and Technology, Gaithersburg, MD.

[66] Tuttle, W. D.; Thorington, R. L.; Viehland, L. A.; Breckenridge, W. H.; Wright, T. G. Interactions of C^+ with Rare Gas Atoms: Incipient Chemical Interactions, Potentials and Transport Coefficients. *Phil. Trans. Roy. Soc. Lond.* **2018**, *376*, 20170145.

[67] Tang, K. T.; Toennies, J. P. An Improved Simple Model for the van der Waals Potential Based on Universal Damping Functions for the Dispersion Coefficients. *J. Chem. Phys.* **1984**, *80*, 3726–3741.

[68] See, for example: Stone, A. J. *The Theory of Intermolecular Forces*; Clarendon Press: Oxford, 1996.

[69] Koutselos, A. D.; Mason, E. A. Correlation and Prediction of Dispersion Coefficients for Isoelectronic Systems. *J. Chem. Phys.* **1986**, *85*, 2154–2160.

[70] Sahoo, B. K.; Timmermans, R. G. E.; Das, B. P.; Mukherjee, D. Comparative Studies of Dipole Polarizabilities in Sr^+, Ba^+, and Ra^+ and Their Applications to Optical Clocks. *Phys. Rev. A* **2009**, *80*, 062506.

[71] Patil, S. H.; Tang, K. T. Multipolar Polarizabilities and Two- and Three-Body Dispersion Coefficients for Alkali Isoelectronic Sequences. *J. Chem. Phys.* **1997**, *106*, 2298–2305.

[72] Sahoo, B. K.; Das, B. P.; Chaudhuri, R. K.; Mukherjee, D.; Timmermans; R. G. E.; Jungmann, K. Investigations of Ra^+ Properties to Test Possibilities for New Optical-Frequency Standards. *Phys. Rev. A* **2007**, *76*, 040504(R).

[73] Soldán, P.; Lee; E. P. F.; Wright, T. G. Static Dipole Polarizabilities (α) and Static Second Hyperpolarizablities (γ) of the Rare Gas Atoms (He–Rn). *Phys. Chem. Chem. Phys.* **2001**, *3*, 4661–4666.

[74] LeRoy, R. J.; Bernstein R. B. Dissociation Energies of Diatomic Molecules from Vibrational Spacings of Higher Levels: Application to the Halogens. *Chem. Phys. Lett.* **1970**, *5*, 42–44.

[75] Le Roy, R. J.; Bernstein, R. B. Dissociation Energies and Long-Range Potentials of Diatomic Molecules from Vibrational Spacings: The Halogens. *J. Molec. Spectrosc.* **1971**, *37*, 109–130.

[76] LeRoy, R. J.; Bernstein, R. B. Dissociation Energy and Long-Range Potential of Diatomic Molecules from Vibrational Spacings of Higher Levels. *J. Chem. Phys.* **1970**, *52*, 3869–3879.

[77] See, for example, Cremer, D.; Kraka, E. Chemical Bonds without Bonding Electron Density – Does the Difference Electron-Density Analysis Suffice for a Description of the Chemical Bond? *Angew. Chem. Int. Ed. Engl.* **1984**, *23*, 627–628.

[78] Gagliardi, L.; Pyykkö, P. Cesium and Barium as Honorary *d* Elements: CsN_7Ba as an Example. *Theor. Chem. Acc.* **2003**, *110*, 205–210.

[79] Wu, X.; Zhao, L.; Jiang, D.; Fernández, I.; Berger, R.; Zhou, M.; Grenking, G. Barium as Honorary Transition Metal in Action: Experimental and Theoretical Study of $Ba(CO)^+$ and $Ba(CO)^-$. *Angew. Chem.* **2018**, *130*, 4038–4044.